

Confidential manuscript submitted to *JGR: Solid Earth*

Geometry and Evolution of Wrench Tectonics in the NE Lau Basin

M. O. Anderson¹, C. Norris-Julseth¹, K. H. Rubin², K. Haase³, M. D. Hannington^{4,5}, A.T. Baxter⁴, and M. S. Stewart^{4†}

¹Department of Earth Sciences, University of Toronto, 22 Russell Street, Toronto, Ontario, M5S 3B1, Canada

²Department of Geology and Geophysics, SOEST, University of Hawaii, 1680 East-West Road, Honolulu, Hawaii, 96822, USA

³GeoZentrum Nordbayern, Friedrich-Alexander University of Erlangen-Nürnberg, Schlossgarten 5, D-91054 Erlangen, Germany

⁴Department of Earth Sciences, University of Ottawa, 25 Templeton, Ottawa, Ontario, K1N 6N5, Canada

⁵GEOMAR, Helmholtz Centre for Ocean Research Kiel, Wischhofstrasse 1-3, 24148 Kiel, Germany

Corresponding author: Melissa O. Anderson (melissao.anderson@utoronto.ca)

[†]Current address: Department of Earth and Environmental Sciences, Mount Royal University, 4825 Mount Royal Gate SW, Calgary, Alberta, T3E 6K5, Canada

Key Points:

- NE Lau basin is dominated by strike-slip kinematics associated with reactivation of pre-existing extensional faults
- Seamount collision segmented the forearc and induced a counter-clockwise rotation of the stress field in the back-arc
- Riedel shearing promotes distributed rear-arc volcanism, in contrast to typical ridge-centered back-arc volcanism

Abstract

The transition from subduction to transform motion along horizontal terminations of trenches is associated with tearing of the subducting slab and wrench tectonics in the overriding plate. One prominent example is the northern Tonga subduction zone, where the influence of wrench tectonics is indicated by abundant strike-slip faulting in the NE Lau back-arc basin. We explore the back-arc dynamics of this region for the first time through structural lineament analyses and kinematic analyses interpreted from ship-based multibeam bathymetry and Centroid-Moment Tensor data. Our results indicate two distinct sets of Riedel shear structures that are associated with a counter-clockwise rotation in the stress field. We propose that this rotation is driven by the collision of the previously unstudied Capricorn Seamount(s). The strain of this collision was accommodated by right-lateral slip along the adjacent crustal scale fault, known as the Fonualei Discontinuity, which segmented the fore-arc. Internal deformation of the northern tectonic block may have been enhanced by friction along the northern boundary imparting westward-directed stress. This study highlights the importance of non-rigid plate kinematics and extensive re-activation of pre-existing faults in this region. Importantly, these structures directly control the development of complex volcanic-compositional provinces, which are characterized by variably-oriented spreading centers, off-axis volcanic ridges, extensive lava flows, and point-source rear-arc volcanoes that sample a heterogeneous mantle wedge, with sharp gradients and contrasts in composition and magmatic affinity. This study adds to our understanding of the influence of subduction-transform motions and terrane collisions on the structural and magmatic evolution of back-arcs.

Keywords

NE Lau Basin; back-arc; wrench tectonics; seamount collision; Riedel shear; bathymetry

1 **1. Introduction**

2 Back-arc basins are extensional features formed behind subduction zones by progressive
 3 rifting of volcanic arcs until passive mantle upwelling creates new oceanic crust (Karig, 1970).
 4 Their initiation is triggered by either processes of hinge-rollback (Chase, 1978; Scholz &
 5 Campos, 1995), and/or slab anchoring on the trenchward side of the upper plate (Heuret &
 6 Lallemand, 2005). Once back-arc spreading is established, it may continue regardless of the
 7 motion of the overriding plate (Sdrolias & Müller, 2006). Movement of the overriding plate
 8 relative to the arc and subduction zone leads to a diverse arrangement of plates and deformation
 9 styles within the near-arc and back-arc environments (Heuret & Lallemand, 2005).

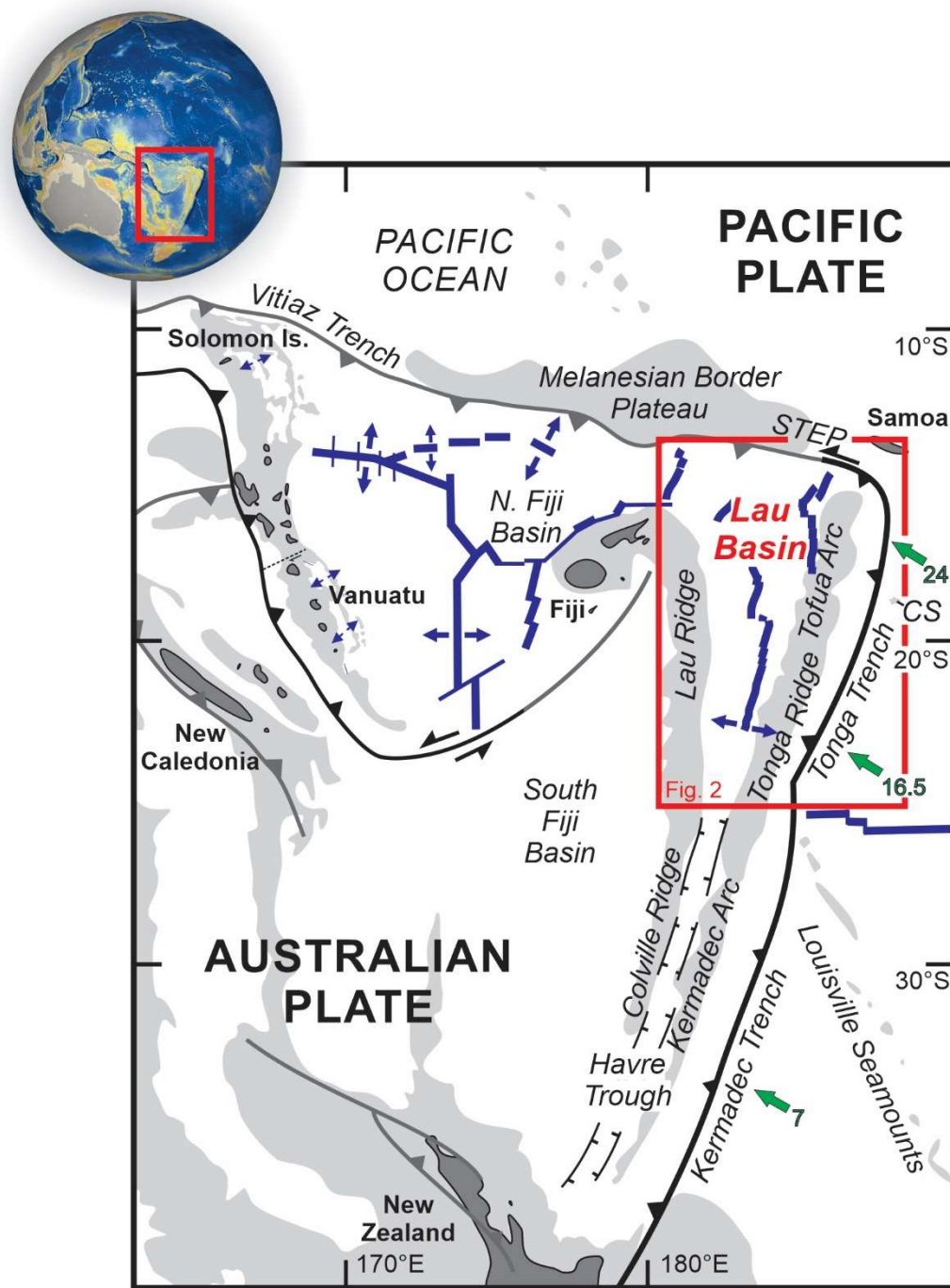
10 The process of hinge-rollback is often disrupted by terrane collisions, where topographic
 11 features on the subducting plate, such as seamounts or oceanic plateaus, can cause a subduction
 12 zone to become temporarily “clogged” or permanently “locked” due to compressional forces on
 13 the arc exerted by the seamount (e.g., Ruellan et al., 2003; Anderson et al., 2016; Mallard et al.,
 14 2016). This in turn may induce oblique subduction and strike-slip tectonics at the edge of the
 15 overriding plate (Ruellan et al., 2003). This can alter the stress field causing plates to rearrange,
 16 triggering rift propagation and the creation of new microplate boundaries in the back-arc (Hey et
 17 al., 1995; Wallace et al., 2005; Zellmer & Taylor, 2001). Edge-driven kinematics are common
 18 along the boundaries of microplates, where microplate rotation is driven by the motion of the two
 19 larger plates the microplate is pinched between (Schouten et al., 1993). These microplate
 20 rotations can cause block rotations, shearing, and further rift propagation (e.g., Easter
 21 Microplate: Neves et al., 2003).

22 Hinge-rollback, seamount subduction, microplate interactions, and variations in trench
 23 geometry and/or subduction angle all influence the state of stress in the overriding plate, driving

24 upper mantle flow and magmatic upwelling, and the formation of structures that provide
25 pathways for magma to reach the surface. This paper focuses on the recent kinematic evolution
26 of the NE Lau Basin, which is one of the most volcanically- and tectonically-active places on
27 Earth (Embley et al., 2009; Rubin et al., 2013; Embley & Rubin, 2018). A combination of
28 remote-predictive geological and structural maps based on high-resolution multibeam
29 bathymetry collected by the *R/V Falkor* expedition FK171110 in 2017 and *R/V Sonne* expedition
30 SO-263 in 2018, compiled with previously-collected bathymetry, are used to interpret the
31 volcanic and structural evolution of the area, providing insight into geodynamic controls on
32 back-arc development.

33 **2. Tectonic Setting**

34 The Tonga-Kermadec subduction zone in the western Pacific extends over 2000 km from
35 New Zealand to Fiji, where the Pacific Plate subducts westward beneath the Indo-Australian
36 Plate (**Fig. 1**). The subduction zone is segmented into the Tonga Trench north of 26°S
37 (associated with the Tofua segment of the Tonga arc) and the Kermadec Trench to the south.
38 Subduction rates along the northern Tonga Trench are the fastest on Earth, with rates of up to
39 240 mm yr⁻¹ sustained for the past 0.78 m.y. (Bevis et al., 1995; Zellmer & Taylor, 2001). There
40 is a southward decrease in subduction rates to 60 mm yr⁻¹, associated with increasing
41 convergence angle obliquity (Bevis et al., 1995). The subducting slab dips uniformly and steeply
42 at about 50° until it meets the northern termination of the subduction zone where it dips more
43 shallowly (Millen & Hamburger, 1998; Hall & Spakman, 2002). Here, a sharp bend to a
44 westerly-direction is associated with a transition from subduction to transform motion, forming a
45 Subduction-Transform-Edge-Propagator (STEP) boundary (Govers & Wortel, 2005).

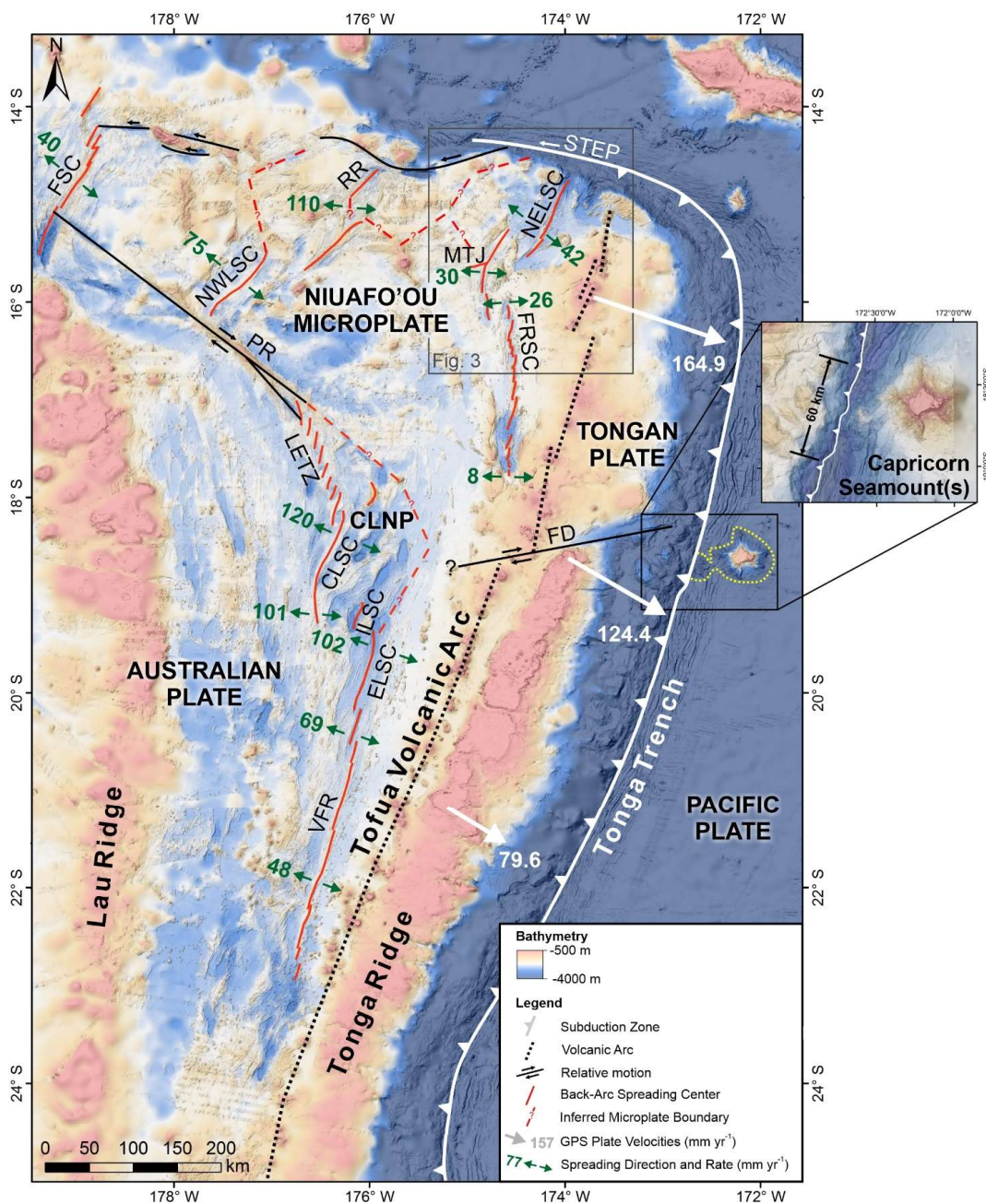


46
 47 **Figure 1.** Geographic location and tectonic features of the southwest Pacific modified from Hall (2002).
 48 Light grey areas represent the 2000 m isobaths, green arrows indicate convergence directions and rates (cm
 49 y⁻¹) from Bevis et al. (1995), and blue lines represent spreading centers. CS = Capricorn Seamount(s), STEP
 50 = Subduction-Transform-Edge-Propagator boundary.

51 This boundary is associated with vertical tearing that causes a piece of the subducting plate to
52 remain at surface (Nijholt & Govers, 2015).

53 Rifting of the northern volcanic arc at 5.5–6 Ma formed the Lau Basin (**Fig. 2**), which
54 evolved to mature seafloor spreading at ca. 5 Ma (Wiedicke & Collier, 1993; Taylor et al., 1996).
55 As the Tonga Trench migrated eastward, arc volcanism shifted from the remnant Lau Ridge to
56 form the new Tofua Arc at 3.5 Ma (Tappin et al., 1994). In the southern part of the subduction
57 zone, rifting of the Kermadec Arc at ca. <2 Ma produced the Havre Trough (Wysoczanski et al.,
58 2019). Unlike the Lau Basin to the north, the Havre Trough is not thought to be undergoing
59 passive mantle upwelling and mature seafloor spreading (e.g., Todd et al., 2010; Tontini et al.,
60 2019).

61 The modern Lau Basin displays a tapering V-shape with a width of ~500 km in the north,
62 narrowing to 200 km in the south where it merges with the Havre Trough (**Fig. 2**). There is a
63 trend of increasing tectonic complexity northward in the Lau Basin (Sleeper & Martinez, 2016).
64 In the south, two plates (Tongan and Australian) are separated by a single segmented spreading
65 center. In the north, the Niufo'ou Microplate has been interpreted to occur between the Tongan
66 and Australian plates, although it is bounded by and contains numerous small spreading centers
67 and propagating rifts, and so structurally might be even more complex (i.e., multiple
68 microplates). There are likely several other micro- or nano-plates in the northern basin with
69 poorly-defined (possibly diffuse) boundaries that have not been studied in detail (Zellmer &
70 Taylor, 2001; Phillips, 2003; Conder & Wiens, 2011). The formation of microplates may be
71 related to processes involving ultrafast opening rates, northward extension, or edge-driven
72 kinematics along the STEP boundary (Conder & Wiens, 2011; Sleeper & Martinez, 2016). Plate
73 reconstructions by Sleeper and Martinez (2016) suggest that non-rigid plate behavior may



74

75 **Figure 2.** Tectonic features and regional bathymetry of the NE Lau Basin compiled from Rubin et al. (2010;
 76 2018), Martinez et al. (2013), Haase et al. (2018) and GEBCO compilation group (2019). Inferred
 77 microplate boundaries based on seismicity from Conder and Wiens (2011), GPS velocities of Tonga relative
 78 to Australia from Phillips (2003) and spreading directions and rates (mm yr^{-1}) for the FSC from Pelletier et
 79 al. (2001), for the NWLSC and RR from Lupton et al. (2015) following Bird (2003), and for the CLSC,
 80 ELSC, FRSC, LETZ, MTJ, NELSC, and VFR from Sleeper and Martinez (2016). CLNP = Central Lau
 81 Nano-Plate; CLSC = Central Lau Spreading Center; ELSC = Eastern Lau Spreading Center; FD = Fonualei
 82 Discontinuity; FRSC = Fonualei Rift and Spreading Center; FSC = Futuna Spreading Center; ILSC =
 83 Intermediate Lau Spreading Center; LETZ = Lau Extensional Transform Zone; MTJ = Mangatolu Triple
 84 Junction; NELSC = North-East Lau Spreading Center; NWSC = North-West Lau Spreading Center; PR =
 85 Peggy Ridge; RR = Rochambeau Rifts; VFR = Valu Fa Ridge.

86 be important in this area, where plate boundaries can propagate and rotate, and experience
87 intraplate deformation.

88 South of the NE Lau Basin study area, seamount subduction also plays an important role
89 in tectonic evolution of the arc and back-arc. The Louisville Seamount Chain (LSC) is colliding
90 with the subduction zone at 26°S, inducing compression and rotation of the volcanic arc, and
91 effectively stalling subduction and back-arc spreading in the southern basin (**Fig. 1**; Ruellan et
92 al., 2003; Wallace et al., 2004; Stratford et al., 2015). At 18°30'S, a partially-subducted portion
93 of the Capricorn Seamount (or seamounts) is indicated by irregular topography rising ~3800 m
94 above the adjacent trench (**Fig. 2**). This collision zone has not been studied in depth but may
95 have an effect similar to the LSC. Opposite the colliding seamount is an area of raised, flat-
96 topped marine terraces in the forearc—a typical feature associated with seamount subduction—
97 forming the Tonga Ridge. Immediately to the north of the collision zone is a large fault zone in
98 the overriding plate called the Fonualei Discontinuity (FD), oriented at a high angle to the trench.
99 This fault extends WSW from the fore-arc and offsets the arc by up to ~40 km. Previous authors
100 suggest that the FD could be related to the initial collision zone with the LSC (e.g., Bonnardot et
101 al., 2007), but the relationship with the collision of the Capricorn Seamount(s) has not yet been
102 investigated. A second, smaller fault has been interpreted at 16°S, offsetting the arc by ~28 km
103 (e.g., Baker et al., 2019); however, there is no surface expression of this fault and this offset may
104 instead reflect the spacing of en echelon segments of the arc.

105 This dynamic tectonic setting results in several distinct attributes among modern-day
106 intra-oceanic subduction zones, including the fastest convergence and back-arc opening rates
107 (Bevis et al., 1995; Embley & Rubin, 2018), highest upper mantle temperatures (Conder &
108 Wiens, 2006), one of Earth's coolest slab parameters and among the highest slab water fluxes

109 (van Keken et al., 2011). We explore the complex structural evolution of the NE Lau Basin—
110 where these processes are the most pronounced—to understand the links between regional
111 geodynamics, microplate tectonics, and magmatic-hydrothermal activity in this unique natural
112 laboratory.

113 **3. Methods**

114 Ship-based multibeam bathymetric data from the NE Lau Basin were collected during
115 two R/V Kilo Moana cruises in 2010 (KM1024; Rubin et al., 2010) and 2011 (KM1129;
116 Martinez et al., 2013), and are supplemented here with new data from R/V Falkor cruise
117 FK171110 in 2017 (Rubin et al., 2018), and R/V Sonne cruise SO-263 in 2018 (Tonga Rift:
118 Haase et al., 2018). The R/V Kilo Moana and R/V Sonne are equipped with Kongsberg EM 122
119 multibeam echo sounders with operating frequencies of 12 kHz, and the R/V Falkor is equipped
120 with a Kongsberg EM 302 multibeam echo sounder with an operating frequency of 30 kHz. The
121 combined surveyed area is 40,760 km², covering 73% of the map area (**Fig. S1**). The raw data
122 were cleaned and gridded at cell sizes of 30 to 50 m by the various shipboard scientific parties.
123 The data were compiled together with the 2019 GEBCO grid (GEBCO Compilation Group,
124 2019) and reprocessed using the “Terrain Texture Shading” (TTS) technique developed by
125 Brown (2014) as an interpretive tool in applied geomatics to reveal subtle surface and structural
126 features that can be directly correlated with seafloor geomorphology (e.g., Augustin et al., 2016;
127 Anderson et al. 2016; 2017).

128 The processed bathymetric maps are interpreted here together with acoustic backscatter
129 data from SO-263 and FK171110 to create a new remote-predictive geological map of the NE
130 Lau basin, following the criteria outlined by Anderson et al. (2016; 2017) and Klischies et al.
131 (2019). Lithological data from ROV sampling, TV grabs (visually aided ship-based scoop

132 sampling), and wax coring from the SO-263 cruise and a compilation of data from literature was
133 used to inform the geological maps (**Fig. S1**). In addition to lithological units, fully
134 georeferenced measurements of structural features, including faults, volcanic ridges, and
135 lineaments are interpreted and digitized. Relative ages of the mapped units were established from
136 overlapping and cross-cutting relationships, and morphological and backscatter evidence of
137 young volcanic flow features and sediment cover.

138 Further “ground-truthing” of the map legend was provided by seafloor observations
139 during ROV dives; seventeen dives were with the MARUM ROV Quest 4000 during the 2018
140 SO-263 cruise, seven dives from the TN234 cruise using WHOI ROV Jason-2 (five dives at
141 West Mata and two dives on the southern NELSC; Resing et al., 2009). The SO-263 QUEST
142 4000 dives included one that transected the wall of the graben in the NE map area that hosts the
143 Niua volcano (Escarpment A), one that transected the northern Tonga forearc, six dives at vent
144 sites at the Niua arc volcano, six dives at various locations around Niutahi volcano, and two
145 dives at the southern NELSC near the Maka seamount and its summit hydrothermal vent site
146 (Haase et al., 2018).

147 Finally, fault kinematics were interpreted from offset features where cross-cutting
148 relationships exist. This was supplemented by centroid-moment tensor (CMT) focal mechanisms
149 from the Harvard CMT catalogue (www.globalcmt.org; Dziewonski et al., 1981; Ekström et al.,
150 2012) for earthquakes with $M_w \geq 5$ and depths of ≤ 25 km. To determine the correct fault-plane
151 solution, each CMT was interpreted in the context of the dominant lineament orientation (**Fig.**
152 **S2**). The CMTs were classified according to type and orientation, following the classification of
153 lineaments. Fault planes were plotted as stereonets to check for consistency in the groupings
154 (**Fig. S3**). This technique has been used since scientists first started recording seismic moments

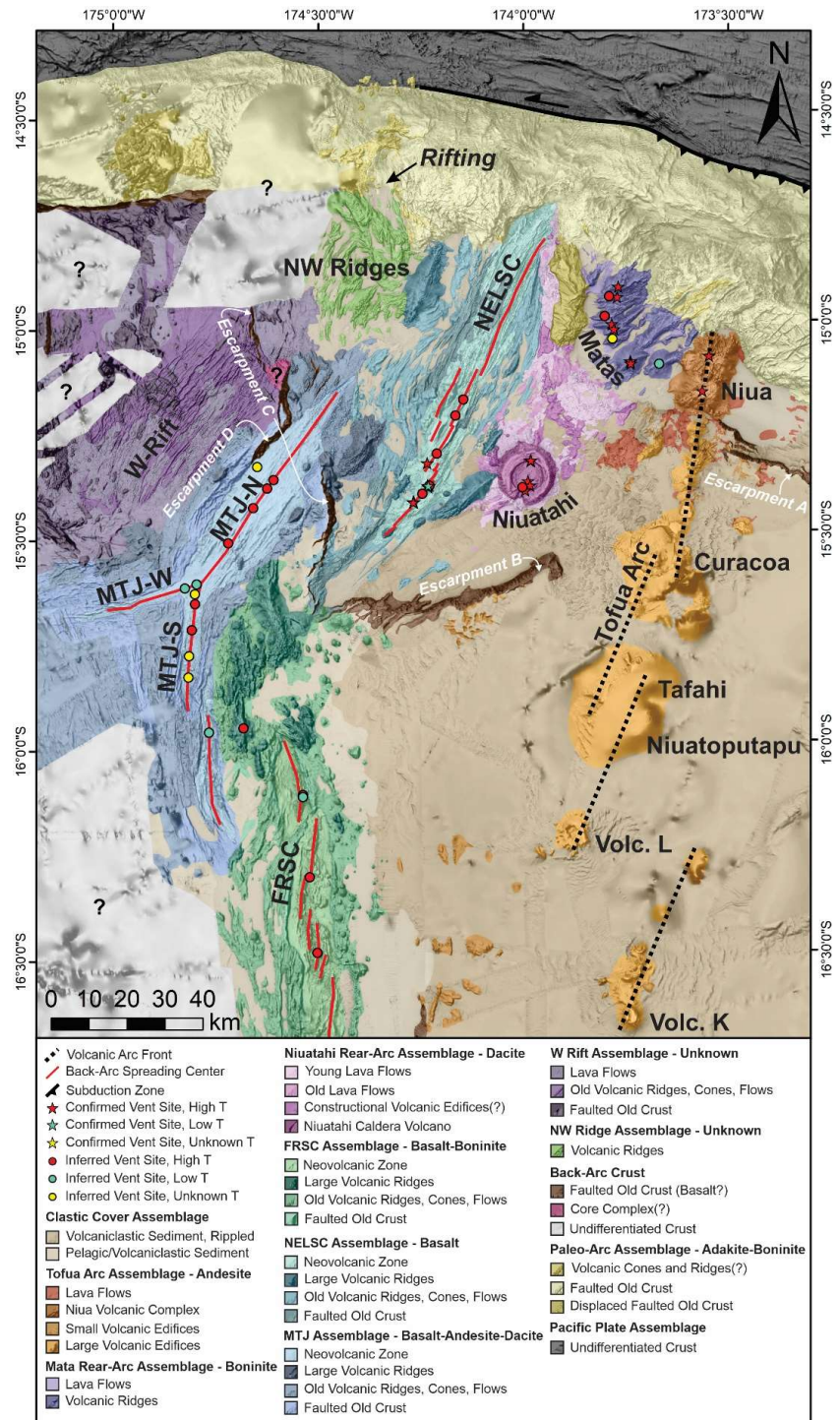
155 (e.g., Mckenzie, 1969) and has been recently applied to understanding changing stress regimes in
 156 the Lau Basin at a regional scale (Baxter et al., submitted).

157 **4. Geological and structural features of the NE Lau Basin**

158 Most of the prior work towards understanding the geology of the Lau Basin has been
 159 focused on the southern basin along the Eastern and Central Lau Spreading Centers, where
 160 crustal accretion resembles mid-ocean ridges. This contrasts the processes of crustal accretion in
 161 the NE Lau Basin, where a diffuse system of back-arc extension, short-lived rifts, spreading
 162 centers, jumping ridge crests, and point-source volcanism dominate (Taylor et al., 1996; Embley
 163 et al., 2009). We present new remote-predictive geological and structural maps of the NE Lau
 164 Basin (**Figs. 3 and 4; Table S1**), which highlight the wide variety of rock types, extensive
 165 volcanism, and complex structural fabrics resulting from the dynamic evolution of the area.

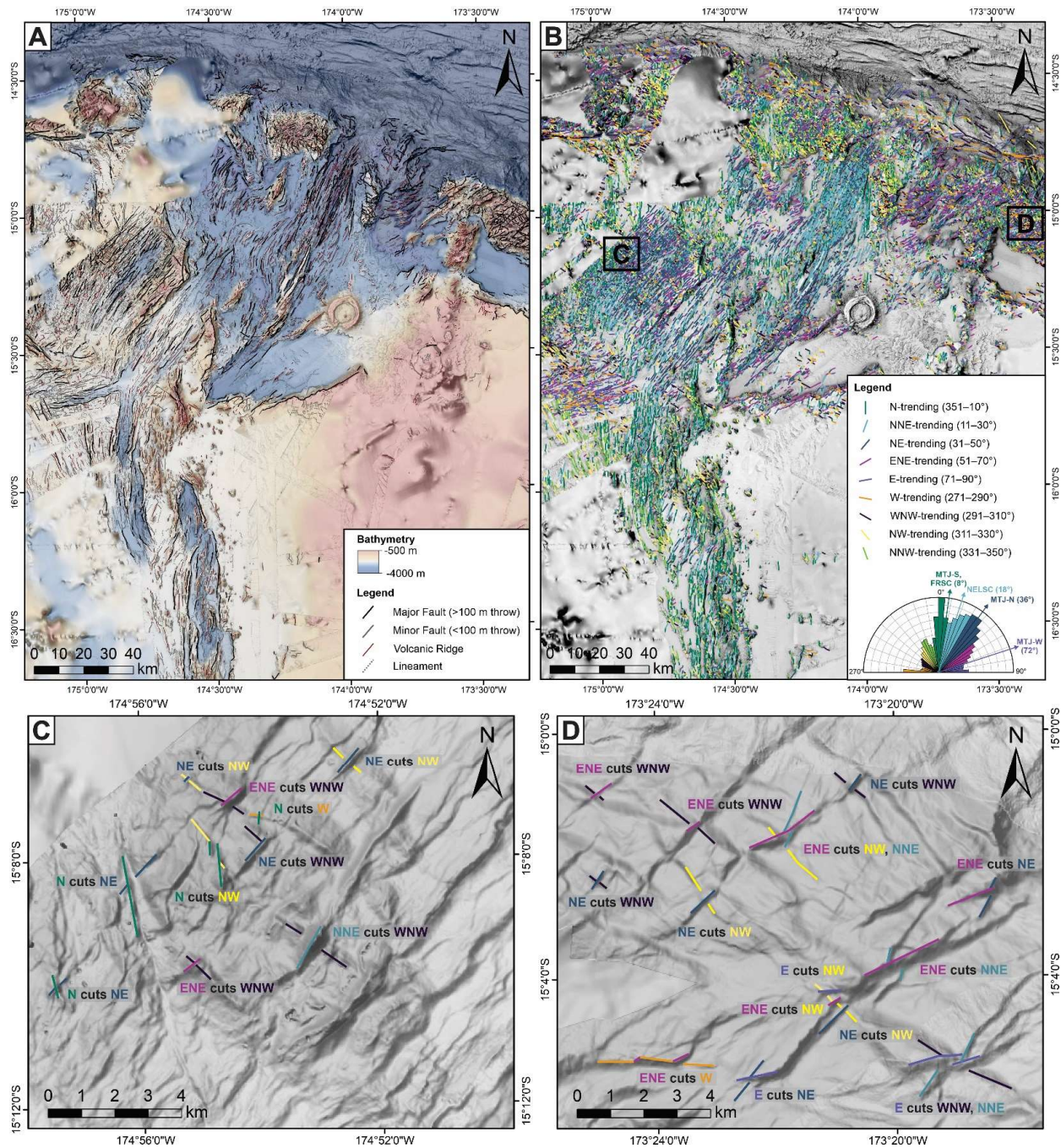
166 4.1. Rifts and spreading centers

167 The spreading centers in the study area include two of the three arms of the Mangatolou
 168 Triple Junction (MTJ; formerly the “Kings Triple Junction”), the North-East Lau Spreading
 169 Center (NELSC), and the northern half of the Fonualei Rift and Spreading Center (FRSC). The
 170 spreading centers primarily erupt basalt, with lesser amounts of basaltic andesite, andesite,
 171 rhyolite, and boninite, with distinct geochemical signatures along each spreading center (Falloon
 172 et al., 2007; Tian et al., 2011; Escrig et al., 2012; Rubin et al., 2018; Haase et al., 2018).
 173 Sampling of the MTJ has revealed a diverse suite of lithologies, spanning the compositional
 174 range from basalt to andesite to dacite (Nilsson et al., 1989; Falloon et al., 1992; Hawkins, 1995;
 175 Langmuir et al., 2006). The NELSC has a mixed geochemical signature of OIB and N-MORB, in
 176 addition to subtle arc-like affinities (Keller et al., 2008; Zhang et al., 2018). Along the southern
 177 MTJ arm and the FRSC, IAB signatures are most abundant, with boninitic



178

179 **Figure 3.** Remote-predicted geological map of the NE Lau basin interpreted from seafloor geomorphology
 180 and limited sampling (**Fig. S1**), overlain on a compilation of ship multibeam bathymetry (from Rubin et al.,
 181 2010; 2018; Martinez et al., 2013; Haase et al., 2018) and the GEBCO 2019 regional bathymetric grid
 182 (GEBCO compilation group, 2019). Hydrothermal vent sites compiled from the FK171111 and SO-263
 183 cruises (Rubin et al., 2018; Haase et al., 2018), InterRidge Vents Database v. 3.4 (Beaulieu & Szafranski,
 184 2019), and Baker et al. (2019). Abbreviations as in **Fig. 2**. Additional details on map units outlined in **Table**
 185 **S1**.



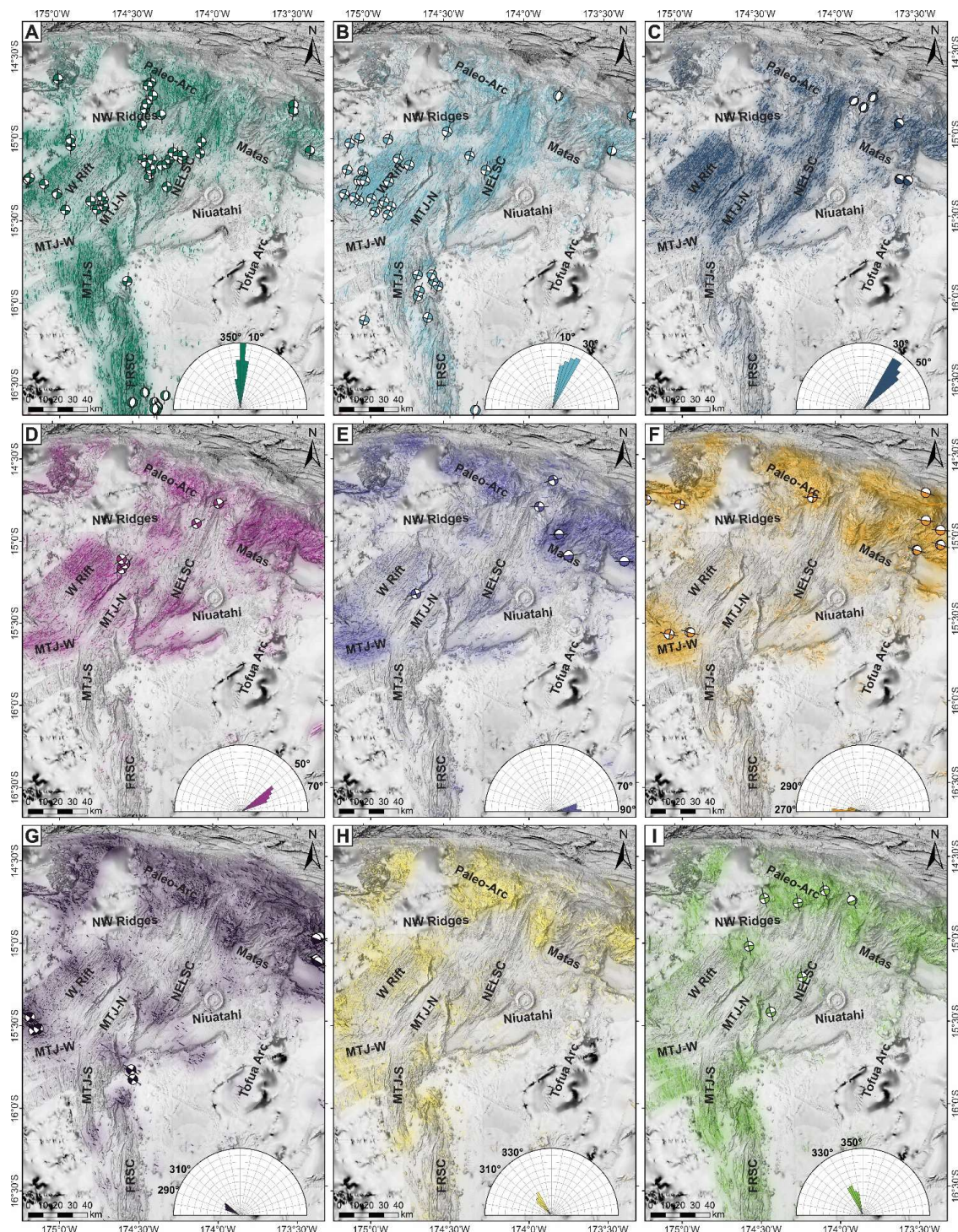
186

187 **Figure 4.** Interpreted structural lineaments in the NE Lau basin: (a) by type, and (b) by orientation. Close-
 188 ups showing examples of cross-cutting relationships of selected structures for: (c) the NW rift zone, and (d)
 189 the paleo-arc crust, summarized in **Table 1**. Abbreviations and bathymetric data sources as in **Fig. 2**.

190 signatures in the central FRSC associated with magmas captured from the volcanic front (Escrig
191 et al., 2012). Despite the proximity of these spreading centers (~30 km), there is a distinct
192 compositional change between them (e.g., Keller et al., 2008). Therefore, these spreading centers
193 are mapped as separate geological assemblages, each consisting of several units (**Fig. 3**).

194 The MTJ is a ridge-ridge-ridge triple junction with each of the three spreading segments
195 displaying distinct morphologies (**Fig. 3**). The MTJ assemblage consists of a neovolcanic zone
196 along the center of each segment, flanked by older crust that is variably faulted or ridge-like. The
197 western arm (MTJ-W) is oriented ENE, accommodating N-S extension in the basin, and is
198 considered to be a failed rift (Phillips, 2003). This arm has a narrow neovolcanic zone (up to 3
199 km wide) within a flat axial valley and is heavily faulted, with structures that are oriented ENE to
200 E-W (**Fig. 5d–e**). The southern arm (MTJ-S) consists of two spreading segments that are
201 oriented N-S, with an axial valley containing a neovolcanic zone that is up to 5 km wide. This
202 neovolcanic zone is dominated by sheet flows and small fissures. Distal volcanic ridges along the
203 flanks of the MTJ-S extend up to 40 km to the west of the spreading center and are steeper and
204 have more relief than ridges along the other arms. In the northern part of the MTJ-S arm, the
205 ridges are cross-cut by E-W trending faults associated with the MTJ-W arm. The southern part of
206 the MTJ-S arm is dominated by N-trending structures (**Fig. 5a**) with minor NNW-trending
207 structures in the south (**Fig. 5i**). The northern MTJ arm (MTJ-N) is a single NNE- to NE-
208 trending segment with a broad axial valley up to 18 km wide, which contains the neovolcanic
209 zone and is bounded by steep faults. The northern and southern ends of the segment consist of
210 small volcanic ridges up to ~180 m tall. The central part of the segment has higher relief with a
211 broad shield-like morphology, and a subtle axial graben up to ~2 km wide. Intense off-axis
212 volcanism occurs along a large ridge in the north (centered at 15°18'S, 174°25'W), which is up to

Confidential manuscript submitted to *JGR: Solid Earth*



213
 214 **Figure 5.** Interpreted structural lineaments, relative lineament densities (lineament km per km²), and
 215 shallow (<25 km) CMT focal mechanisms from Harvard (www.globalcmt.org; Dziewonski et al., 1981;
 216 Ekström et al., 2012), classified according to interpreted strike: (a) N-trending (max. 0.57 km/km²), (b)
 217 NNE-trending (max. 1.25 km/km²), (c) NE-trending (max. 1.04 km/km²), (d) ENE-trending (max. 0.64
 218 km/km²), (e) E-trending (max. 0.57 km/km²), (f) W-trending (max. 0.24 km/km²), (g) WNW-trending (max.
 219 0.29 km/km²), (h) NW-trending (max. 0.29 km/km²), (i) NNW-trending (max. 0.33 km/km²). Stereonets of
 220 CMTs grouped according to interpreted strike shown in **Fig. S3**.

221 1300 m tall and 17.5 km long, and an area with large, low-relief cratered volcanoes to the NW of
222 the triple junction (centered at 15°30'S, 174°57'W).

223 To the west of the MTJ-N arm is an area of rifting with inward-dipping faults and no
224 associated neovolcanic zone, which we refer to as the Western Rift assemblage. In the north, the
225 crust is heavily faulted with overlapping zig-zag structures that trend NNE, NE, and ENE
226 (**Fig. 5b–d**). In the south, the crust is dominated by younger volcanic flows with morphologies
227 characteristic of sheet flows with collapse features and lesser amounts of pillow flows. Volcanic
228 flows become more common to the west towards the subaerial Niuafou'ou volcanic island, located
229 outside the study area. Cross-cutting the dominant NE-fabric of this area are WNW- and NW-
230 trending volcanic ridges and faults (**Fig. 5g–h**). The area has not been previously described or
231 sampled, and therefore the lithology is unknown.

232 The NELSC assemblage follows a NE-oriented spreading center that consists of four
233 segments and displays a gently sigmoidal shape. The northernmost segment is characterized by a
234 40-km long axial valley resembling a slow-spreading MOR morphology, while the remaining
235 segments in the south are characterized by axial ridges that are ~15 km in length resembling fast-
236 spreading MOR morphologies. The neovolcanic zone is irregular, between 3.4 and 9.7 km wide.
237 The neovolcanic zone of the northernmost segment consists of elongate hummocky lava flows
238 and mounds. There is a gradual progression southward towards a more flat-topped axial volcanic
239 ridge morphology with point-source volcanic cones. Flat-topped volcanic cones occur near the
240 ends of the NELSC. The southernmost segment is the most magmatically-robust, with axial
241 volcanic ridge highs reaching ~1260 m above the surrounding seafloor, with large volcanic cones
242 on each termination of the ridge (Maka and Tafu). Proximal to the neovolcanic zone is older,
243 faulted crust, followed by distal heavily-sedimented ridges. These ridges are symmetrical,

244 indicating a volcanic rather than structural origin. Several large volcanic ridges up to 1570 m tall
245 and 24 km long occur distal to the spreading center, notably to the east of the southern NELSC
246 (centered at 15°24'S, 174°08'W) and to the west of the northern NELSC (centered at 14°55'S,
247 174°15'W). The structures along this spreading segment are dominantly NNE- and NE-trending
248 (**Fig. 5b–c**), with distal N-trending structures associated with volcanic ridges on the SW and NE
249 sides of the spreading center (**Fig. 5a**).

250 The FRSC overlaps with the MTJ-S and is oriented N-S to accommodate E-W extension
251 between the Niufo'ou and Tongan microplates (Sleeper & Martinez, 2016). The FRSC consists
252 of at least six overlapping, left-stepping segments that become progressively closer to the arc
253 towards the south, described by Sleeper et al. (2016). The study area includes the three northern
254 segments, which are ~12–27 km long and are characterized by axial valleys containing a
255 neovolcanic zone up to ~15 km wide (**Fig. 3**). Narrow axial volcanic ridges are surrounded by
256 smooth, featureless seafloor that may be sheet flows or volcanoclastic sediment derived from the
257 nearby volcanic arc. The axial valleys are bounded by steep-sided faults, but unlike other
258 spreading segments in the study area, off-axis faulting is not laterally continuous. The valley
259 flanks are dominated by irregular volcanic ridges and numerous small volcanic cones. To the
260 south of the map area, the axial valleys become less pronounced and there is a transition towards
261 axial ridge morphologies. Based on the width of this assemblage (20–30 km) and the inferred
262 spreading rate (26 mm yr⁻¹; Sleeper & Martinez, 2016) at the northern extent of the FRSC, rifting
263 began between 0.8 and 1.1 Ma. In the north there is an area of robust volcanic activity
264 characterized by coalescing volcanic cones and ridges, as well as a large volcanic ridge, 29-km-
265 long and 1350-m-tall, extending towards the MTJ-N (centered at 15°41'S, 174°38'W). The
266 transition between the FRSC and the MTJ-N is difficult to distinguish. The structures along the

267 FRSC are dominantly N-trending (**Fig. 5a**), with minor NNE- and NNW-trending structures at
268 the northern termination (**Fig. 5b and i**).

269 Finally, an enigmatic area consisting of variably-oriented volcanic ridges that are not
270 clearly associated with a spreading center occur in the NW part of the map area, referred to here
271 as the NW Ridge Assemblage (**Fig. 3**). This area may reflect a distal portion of the NELSC. The
272 ridges are sub-parallel and oriented NNE to NE (**Fig. 5b–c**) and WNW to NNW (**Figs. 5h–i**).
273 The ridges rise to heights of 760 m above the surrounding seafloor. The areas between the ridges
274 is interpreted to be sediment, although backscatter data is lacking in this area and young lava
275 flows may be present. In the north, the ridges are cut by a N-trending rift that extends into the
276 paleo-arc and appears to be heavily sedimented. The curved appearance of some of the ridges
277 may be related to extension along this rift, resembling a large-scale drag fold. The southern
278 contact between this unit and the NW Rift assemblage is poorly defined due to a lack of high-
279 resolution multibeam and backscatter data and may be gradational. The lithology of this
280 assemblage is unknown because it has not yet been sampled.

281 4.2. Rear-arc volcanism

282 Volcanism that occurs between the active arc front and the spreading centers is referred
283 to as rear-arc volcanism, which is associated with more siliceous lithologies than the back-arc
284 (e.g., Embley & Rubin, 2018). The Mata volcano assemblage occurs in the NE part of the study
285 and consists of nine elongate en echelon volcanic ridges composed of boninitic pyroclastic
286 material and lava flows, surrounded by lava flows (**Fig. 3**; Resing et al., 2011a; Rubin &
287 Embley, 2012). These volcanoes have been actively erupting over the last 2 Ma, with older
288 occurrences extending into the fore-arc region (Falloon et al., 2008; Rubin & Embley, 2016;
289 Chadwick et al., 2019). The southern volcanoes, West and East Mata, are 1400–1700 m tall and

290 are elongate along an ENE-trend (**Fig. 5d**). The West Mata volcano is one of only two places in
 291 the world where deep-sea submarine eruptions have been witnessed (Resing et al., 2011b). The
 292 Mata volcanoes to the north (Taha, Ua, Tolu, Fa, Nima, Ono, Fitu) are smaller (900–1300 m tall)
 293 and are variably elongate in ENE- and E-directions.

294 South of the Mata volcanoes is the Niuatahi assemblage, characterized by the 15-km wide
 295 Niuatahi dacite volcano (formerly “Volcano O”), that rises ~1340 m above the surrounding
 296 seafloor with a 9-km-wide nested caldera (**Fig. 3**). This volcano is cross-cut by a regional N-
 297 trending structure (**Fig. 5a**), with E-W extension indicated by short gaps in the caldera walls in
 298 the north and south (Baker et al., 2019). Along this regional structure in the south-central part of
 299 the caldera is a 465-m-tall resurgent volcanic cone called Motutahi, which is associated with
 300 dacite flows (Park et al., 2015) and active venting (Kim et al., 2009). Niuatahi is surrounded by
 301 dacite lava flows that extend ~60 km north and northeastward over an area of ~640 km²,
 302 described by Embley and Rubin (2018). Backscatter signatures indicate at least two ages of
 303 flows, with the most recent flows displaying a very high backscatter signal. The chemistry of the
 304 flows varies according to location, which Embley and Rubin (2018) use to define three distinct
 305 flows, indicating that the eruptions originate from a fissure rather than simply from the Niuatahi
 306 volcano. At the map scale here, we group the young flows as a single unit. Lower-than-expected
 307 viscosities of these Si-rich lavas are attributed to high magmatic water contents, CO₂ contents,
 308 and/or high eruptive temperatures (Embley & Rubin, 2018). These dacite flows surround
 309 irregularly-shaped topographic features, which we interpret to be older constructional volcanic
 310 features that represent a central fissure system.

311 4.3. Arc volcanism

312 In the study area, the Tofua arc trends $\sim 18\text{--}23^\circ$ in the south and $\sim 5\text{--}8^\circ$ in the north (**Fig.**
313 **3**). This assemblage consists of four units: large arc volcanos (including Volcano L, Volcano K,
314 Niuatoputapu, Tafahi, Curacoa, and other unnamed volcanoes), the Niuia volcanic complex,
315 smaller volcanic edifices, and lava flows. The northern portion of the arc has not been sampled
316 extensively; however, four samples were collected during the SO-263 cruise, including one
317 andesite, two basaltic andesites, and one basalt (Haase et al., 2018). This is consistent with
318 sampling along the arc segment adjacent to the FRSC, which is dominantly basaltic andesite
319 (Keller et al., 2008; Sleeper, 2017). The Tofua arc volcanoes are dominantly submarine
320 stratovolcanoes that decrease in size northwards towards the termination of the arc. Many of
321 these volcanoes have large interior caldera structures. Submarine volcanoes K and L, and
322 subaerial volcano Niuatoputapu are all apparently inactive. No historical eruptions have been
323 reported at subaerial Tafahi volcano, but the youthful morphology suggests recent (Holocene)
324 activity (Taylor & Ewart, 1997). A recent eruption at the submarine Curacoa volcano was
325 reported in December 1979 (Global Volcanism Program, 2013). At the northern termination of
326 the arc, the submarine Niuia volcanic complex (formerly “Volcano P”) has a distinct morphology
327 consisting of numerous overlapping cones and a strongly tectonized appearance. This large
328 complex appears roughly rectangular in plan view, up to 25 km long and 13 km wide, and rises
329 to depths of ~ 2000 m above the surrounding seafloor. Small (≤ 100 m tall), dome-like
330 topographic features that are irregularly distributed at the top of the Niuia complex are interpreted
331 to be small volcanic edifices. Profuse venting of S-rich magmatic fluids at the Niuia North vent
332 site indicate that it is volcanically active (Rubin et al., 2018; Haase et al., 2018). Niuia is the only
333 place along the Tofua arc in the map area that has confirmed hydrothermal venting (Niuia South
334 vent field; Arculus, 2004). Surrounding the northernmost arc volcanoes are young lava flows that

335 are identified by high backscatter signatures. We interpret these flows to be genetically related to
336 the Tofua arc volcanoes based on proximity; however, these flows have not been sampled so this
337 relationship is unconfirmed.

338 4.4. Paleo-arc crust

339 The paleo-arc assemblage occurs in the northernmost part of the map area and is
340 characterized by a bulging morphology that is heavily tectonized (**Fig. 3**). We include the paleo-
341 fore-arc with this assemblage as the morphology does not allow easy distinction. Few samples
342 from this area have been collected, mainly consisting of adakite and boninite (Falloon et al.,
343 2008; Price et al., 2016). The density of structures in this area is high and includes structures of
344 every orientation (**Fig. 5**). There are some areas adjacent to active back-arc volcanism where the
345 paleo-arc appears to contain volcanic ridges and cones with youthful morphologies that may be
346 capturing magmatism from the back-arc. Backscatter data in these areas is lacking and samples
347 have not been collected. In addition, an area of intensely-faulted terrane to the west of the Mata
348 volcanoes is interpreted to be an area of detached paleo-arc crust. The structural fabric of this
349 block is dominated by WNW-, NW- and NNW-trending fabrics, similar to the paleo-arc crust on
350 the opposite side of the NELSC (**Figs. 5g-i**), and distinct from adjacent assemblages. However,
351 these structural orientations may have been modified during opening of the NELSC, and so the
352 origin remains uncertain. This displaced unit does not show evidence of recent volcanism.

353 4.5. Sedimentary features

354 Clastic sediments are ubiquitous throughout the basin (**Fig. 3**), forming a cover sequence
355 that is divided into two units: a rippled volcanoclastic sediment apron that extends from the
356 volcanic arc, and a smooth featureless plain that is likely a combination of pelagic and

357 volcanoclastic sediment. The contact between these two units is gradational, and the contacts
 358 with other units tends to be sharp and can be distinguished by the very low backscatter signature.

359 4.6. Structural features

360 A total of 5,892 major fault segments (>100 m throw), 12,071 minor fault segments (<
 361 100 m throw), 7,420 volcanic ridge segments, and 10,624 lineament segments were interpreted
 362 and digitized (**Fig. 4**). The distribution of the structural orientations is shown in **Figure 5**. The
 363 dominant orientations are N-trending (0–10°; $n = 2959$) and NE-trending (30–40°; $n = 3033$),
 364 following the orientations of the major spreading centers. Evidence for cross-cutting
 365 relationships between the structures is most pronounced in highly tectonized areas, namely, the
 366 W Rift zone and the Paleo-Arc crust (**Fig. 5**). Cross-cutting relationships between structures with
 367 similar orientations (e.g., N- and NNE-trending) were not observed, instead these features tend to
 368 form zig-zag faults. A summary of relative cross-cutting relationships is outlined in **Table 1**,
 369 with examples shown in **Fig. 4c, d**. In general, these relationships indicate that the oldest
 370 structures are NNW-, NW-, and WNW-trending, intermediate-age structures are NE- and NNE-
 371 trending, and the youngest structures are N-, W-, E-, and ENE-trending.

372 4.7. Escarpments

373 There is a distinct three-tiered down-dropped basin topography across the NE Lau Basin
 374 (**Fig. 2**). The borders of these tiers are defined by large escarpments with throws of up to 1500
 375 m, which are some of the most striking features in the basin (**Figs. 3 and 4a**). A large escarpment
 376 in the NE map area (“Escarpment A” in **Fig. 3**) forms the wall of the ~NNW-trending basin that
 377 hosts the Mata volcanoes and the Niua arc volcano. This escarpment is ~30 km long in the map
 378 area and has a maximum throw of 890 m. The dip of this escarpment is variable across its length,
 379 averaging 36° to the NNE. One dredge sample from this escarpment was dated at 2.03 ± 0.11 Ma

380 **Table 1.** Cross-cutting relationships of structures according to orientation (examples in **Fig. 4c, d**)

Structure by orientation	Cross-Cut By	Cross-Cuts	Shear Sense
NNW-trending	N, NNE, NE, E, W		
NW-trending	N, NNE, NE, ENE, E		
WNW-trending	N, NNE, NE, ENE, E		
NE-trending	N, ENE, E, W	WNW, NW, NNW	Unknown (offset minor)
NNE-trending	ENE, E	WNW, NW, NNW	R-lateral
N-trending	W	NE, NNW, WNW, NW, W	R-lateral
W-trending	N, ENE	N, NE, NNW	L-lateral
E-trending		NNE, NE, NNW, WNW, NW	L-lateral
ENE-trending		NNE, NE, WNW, NW, W	L-lateral

381

382 (K-Ar dating; Falloon et al., 2007), although the timing of formation of this escarpment is
 383 difficult to constrain due to its association with recent volcanic flows (**Fig. 3**). Another ~62-km-
 384 long escarpment with a maximum throw of 1070 m occurs at the southern termination of the
 385 NELSC (“Escarpment B” in **Fig. 3**) trending ~ENE towards the arc. The average dip is 24° to the
 386 NW. Connected to this escarpment in the south is a ~N trending escarpment (“Escarpment C” in
 387 **Fig. 3**) that becomes NNE-trending with increasing latitude. This escarpment extends ~37 km
 388 before it is interrupted by the MTJ-N at 15°19’S. It continues on the opposite side for another
 389 ~38 km. This part of the escarpment appears to be interrupted by a detachment fault at 15°07’S
 390 (mapped as a core complex in **Fig. 3**), characterized by NNW-trending corrugations, although
 391 there is a high degree of uncertainty in the identification of this feature. This escarpment appears
 392 to comprise multiple stepping faults in places, but in general it has a maximum throw of 1095 m,
 393 dipping ~24° to the E and NE. It is intersected by an NNW-trending escarpment (“Escarpment
 394 D” in **Fig. 3**) that forms the western boundary of the MTJ-N. This escarpment has a maximum
 395 throw of 1085 m, decreasing in size southwards towards normally-faulted terrain of the MTJ.
 396 Using a cutoff throw of 500 m to define this escarpment, it has a length of ~23 km, and dips of
 397 22° to the SE. These dip angles are likely an underestimate of the true dips due to erosional
 398 processes over time, indicated by mass wasting features at the base of some of the escarpments.

399 **5. Fault kinematics**

400 Two of the primary forces driving plate kinematics in the NE Lau Basin are: (1) arc-
 401 parallel extension associated with SE rollback of the Tonga trench, and (2) strike-slip movement
 402 associated with asymmetric slab rollback and wrench tectonics along the STEP boundary (e.g.,
 403 Govers & Wortel, 2005; Embley et al., 2009). Extensional rift-parallel horst-and-graben fault
 404 patterns are common across the map area, including within neovolcanic zones and off-axis

405 terrains along the main spreading centers (**Fig. 4a**). Extensional structural fabrics in the NE Lau
406 basin are characterized by two main structural trends that record the recent stages of back-arc
407 development. The first trend is parallel to sub-parallel with the NELSC and MTJ-N (NNE- to
408 NE-trending; **Fig. 5b, c**). This trend follows the orientation of the Tofua arc between 15°30'S and
409 17°35'S, and south of the collision zone with the Capricorn Seamount(s) between 18°32'S and
410 24°0'S (~18–23°; **Figs. 2 and 3**). The second trend is parallel to sub-parallel with the MTJ-S and
411 FRSC (N-trending; **Fig. 5a**). This trend follows the orientation of the Tofua arc north of 15°30'S,
412 and to the north of the Capricorn Seamount(s) collision between 17°35'S and 18°32'S (~5–8°;
413 **Figs. 2 and 3**). Subordinate structures are orthogonal to these trends but also display normal
414 faulting and extensional features, including the NE- and ENE-trending large volcanic ridges near
415 the southern NELSC and within the Mata volcanic group (**Figs. 4 and 5c,d**).

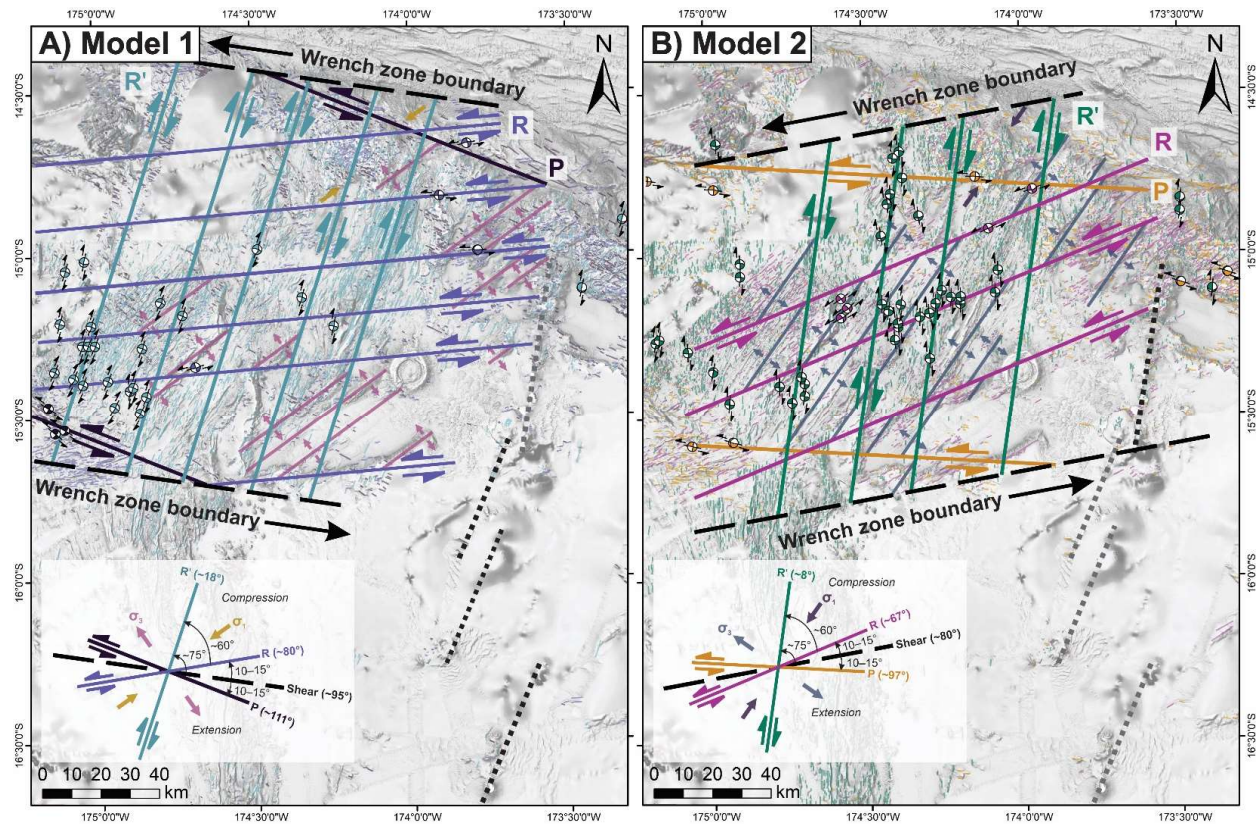
416 Despite the abundance of normal faulting and spreading center development, shallow
417 normal earthquakes are restricted to the FRSC in the south of the map area ($n = 8$; **Fig. 5a**), as
418 well as the northern tip of the NELSC ($n = 4$; **Fig. 5 b, c**). It is likely that extension in the basin
419 is simply not producing high-magnitude ($M_w > 5$) earthquakes. This may indicate that crustal
420 accretion is dominated by magmatic extension driven by dike injection rather than tectonic
421 extension driven by brittle faulting (e.g., Buck et al., 2005; Ito & Behn, 2008; Anderson et al.,
422 2017).

423 Notably, strike-slip and oblique-slip faulting is widespread across the study area, with
424 shear sense indicated by offset features (**Table 1; Fig. 4c, d**) and high-magnitude earthquake
425 focal mechanisms (**Fig. 5**). The main N- and NNE-trending structures (along with minor NNW-
426 trending structures) display a right-lateral shear sense (**Fig. 5a, b, i**), accounting for 73% of
427 shallow strike-slip CMT solutions in the area. In contrast, NE-trending structures do not display

428 strike-slip motion; instead, these structures may be associated with pure low-magnitude normal
429 faulting with no oblique motion. Subordinate NE-, ENE-, E-, W-, NNW-trending structures
430 display a left-lateral shear sense (**Fig. 5d–g**), accounting for 27% of the shallow strike-slip CMT
431 solutions. The left-lateral CMTs occur near the STEP boundary ($n = 7$), likely caused by slip
432 between the northern microplates and the Pacific Plate, and farther to the south along the W Rift,
433 MTJ-W, and northern FRSC ($n = 19$). Dip-slip faults also occur along the STEP boundary east of
434 the NELSC, trending NE, E, W, and WNW ($n = 12$; **Fig. 5c, e–g**).

435 The abundance and distribution of strike-slip faulting supports the null-hypothesis that
436 wrench-tectonics dominate the NE Lau basin—extending as far south as $\sim 16^\circ\text{S}$ where strike-slip
437 CMT solutions terminate abruptly—driven by the left-lateral motion along the plate boundary
438 along with asymmetrical hinge-rollback. There is no evidence for slip along the inferred southern
439 boundary of the wrench zone (dashed lines in **Fig. 6**), which instead is dominated by a diffuse
440 zone of seismicity. This is consistent with other edge-driven microplate rotation models (e.g.,
441 Schouten, 1993).

442 We relate the distribution and orientation of right-lateral and left-lateral strike-slip faults
443 within the rigid block boundaries to Riedel shear mechanisms typical of wrench zones, revealing
444 two distinct sets of structures (**Fig. 6**). The first set of Riedel shears are dominated by NNE-
445 trending R' -shears, with minor E-trending R-shears and NNW-trending P-shears (Model 1: **Fig.**
446 **6a**). The R' -shears are oriented at a high angle ($\sim 75^\circ$) counter-clockwise to the boundaries of the
447 wrench zone, which trend $\sim 95^\circ$ following the orientation of the northern plate boundary. The R' -
448 shears follow the main trends along the NELSC and the W Rift zone and are sub-parallel to
449 MTJ-N. Typically, R' -shears may develop with or after R-shears (e.g., Atmaoui et al., 2006),
450 which are oriented $\sim 10\text{--}15^\circ$ counter-clockwise and synthetic to the wrench zone boundaries. In



451

452 **Figure 6.** Riedel shear mechanisms associated with strike-slip faulting in a wrench zone overlain on
 453 greyscale-shaded bathymetry with associated lineaments, showing two configurations: (a) Model 1, with
 454 shear zone boundaries oriented $\sim 98^\circ$ dominated by NNE-trending R'-shears that are parallel to the southern
 455 Tofua Arc segments, with active seismicity mostly restricted to the western map area, and (b) Model 2,
 456 with shear zone boundaries rotated counter-clockwise to $\sim 80^\circ$ dominated by N-trending R'-shears that are
 457 parallel to the northern Tofua Arc segment, with active seismicity dominating the central map area.
 458 Extension associated with σ_3 is offset by R-shears and is associated with large volcanic ridges across the
 459 map area in both configurations. Bathymetric data sources as in **Fig. 2** and CMT focal mechanisms as in
 460 **Fig. 5**.

461 the study area, R-shears are not widespread, but closely align with the structural trend of the
 462 eastern Mata volcanoes and a well-developed strike-slip fault zone in the northwest map area.
 463 The P-shears are more difficult to identify but may be manifest as the WNW-trending fabrics in
 464 the southern and northern parts of the map area. Within this configuration, compression
 465 associated with σ_1 may produce the bulging morphology of the paleo-arc crust, and extension
 466 associated with σ_3 is associated with the large ENE-trending volcanic ridges at the southern end
 467 of the NELSC, as well as West and East Mata. The orientation of these structures is oblique to
 468 the direction of hinge-rollback, suggesting that normal back-arc spreading processes cannot
 469 account for all the extension in this area. These extensional features are offset by the R-shears,
 470 creating an extensional duplex (**Fig. 5**). North of the FRSC, there appears to be a cluster of NNE-
 471 trending seismicity associated with left-lateral fault motion, contrasting the right-lateral motion
 472 of faults along other NNE-trending CMTs in the region (**Fig. 5b**). Sleeper (2017) suggests that
 473 these strike-slip events are due to a zone of transferred lithosphere, although the regional
 474 kinematic control on this reversal is unclear. We therefore interpret the southernmost diffuse
 475 boundary of the wrench zone to occur near Escarpment B (**Figs. 3 and 6b**).

476 The second set of Riedel shears are similar but rotated $\sim 8\text{--}12^\circ$ counter-clockwise relative
 477 to the first set of shears (Model 2: **Fig. 6b**). These shears are dominated by N-trending R'-shears,
 478 with minor ENE-trending R-shears and W-trending P-shears. The R'-shears follow the
 479 orientation of MTJ-S and FRSC, the N-trending fissure system extending north of the Niuatahi
 480 volcano, and other N-trending features in the area. The R-shears follow the trend of the southern
 481 and eastern Mata volcanoes and the large volcanic ridge to the west of Niuatahi, apparently re-
 482 activating previous extensional fabric. The wrench zone boundaries trend $\sim 80^\circ$, following the
 483 previous orientation of R-shears in Model 1 (**Fig. 6a**), and sub-parallel to the orientation of

484 Escarpment B in the south (dashed lines in **Fig. 6**). Notably, the orientation of the wrench zone
485 parallels the major Fonualei Discontinuity that offsets the arc to the south of the study area (**Fig.**
486 **2**). P-shears are also poorly defined for this configuration, but match strike-slip faulting near the
487 northern and southern boundaries of the wrench zone. In this configuration, extension along σ_3 is
488 associated with NE-trending volcanic ridges across the map area, such as the western Mata
489 volcanoes, which are offset by R-shears. This extensional fabric is also parallel to the MTJ-N,
490 the West Rift zone, and the northern and southern terminations of the NELSC and may be
491 enhancing spreading associated with hinge-rollback.

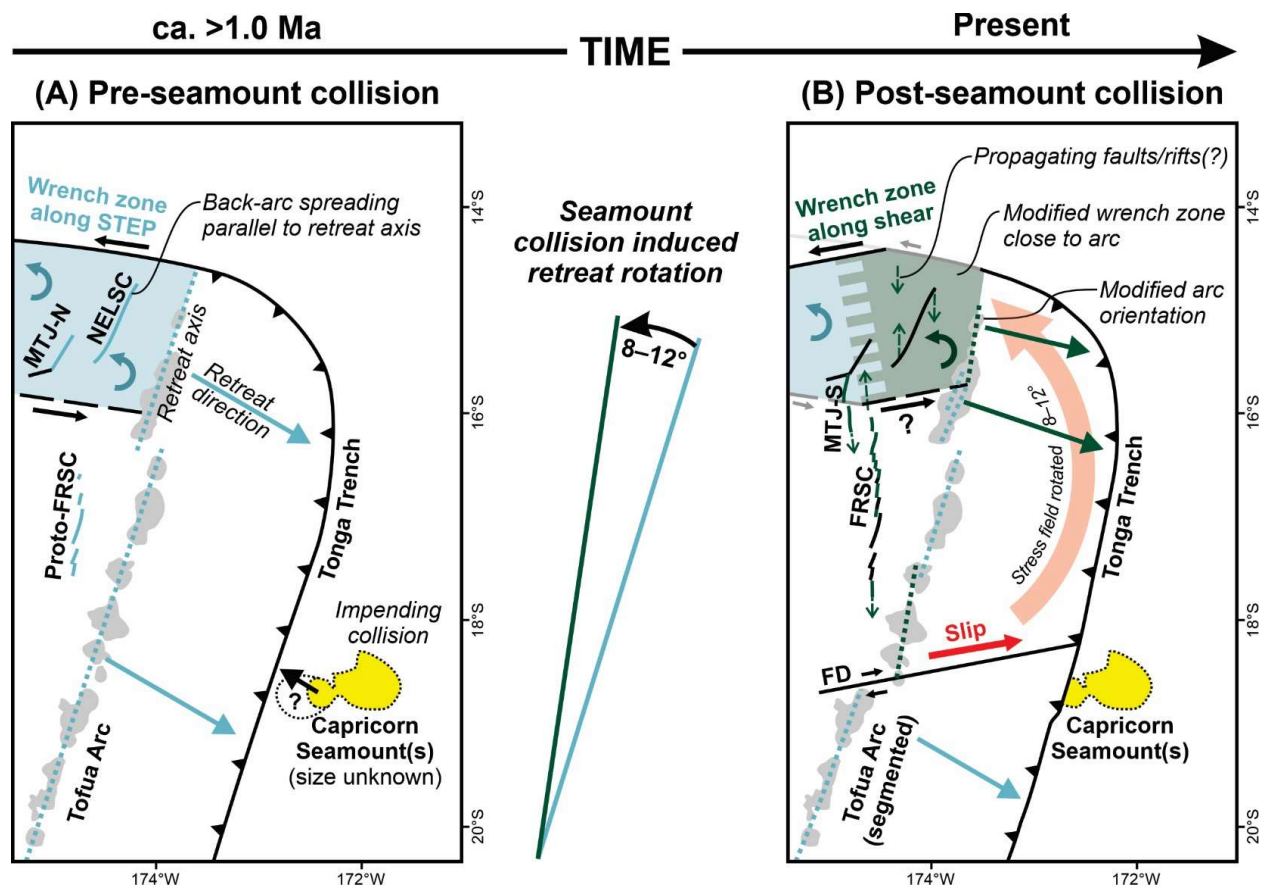
492 The differing distribution of fault populations from a typical Riedel shear zone
493 (dominated by R-shears) is likely because R'-shears occur at an angle similar to that of faults
494 produced by earlier back-arc extension. It is easier to reactivate these pre-existing faults as
495 opposed to creating new ones as the stress required for frictional sliding along pre-existing faults
496 is much less than the fracture strength (e.g., Byerlee, 1978). Similarly, as the stress-field rotated,
497 pre-existing extensional faults were re-activated as R-shears. This effect has been observed in
498 other back-arc basins (e.g., Manus Basin: Martinez & Taylor, 1996; Morley et al., 2004;
499 Maestro-González et al., 2008). Faults that have undergone strike-slip reactivation tend to have
500 zig-zag geometries with little throw. These morphologies are common throughout the map area
501 but are particularly well-defined in the western part of the map area in the West Rift zone and the
502 MTJ-W arm. Therefore, the observed strike-slip kinematics in the study area support a rigid
503 block model of lithospheric-scale Riedel shearing, where shearing reactivates pre-existing
504 extensional faults. This indicates that structures in wrench zones may be predisposed to align
505 themselves to the pre-existing fabrics in back-arc settings.

506 6. Discussion

507 6.1. Tectonic evolution of the NE Lau Basin

508 The occurrence of two different Riedel shear geometries in the NE Lau Basin (Models 1
509 and 2; **Fig. 6**) indicates that the stress field has rotated over time. Structures associated with both
510 geometries are distributed across the map area; however, active seismicity associated with Model
511 1 (dominated by NNE-trending R' -shears) occurs mainly in the western portion of the map area,
512 while seismicity associated with Model 2 (dominated by N-trending R' -shears) occurs in the
513 central portion of the map area closest to the active arc. Cross-cutting relationships indicate that
514 Model 2 structures generally are the youngest (**Table 1**). We propose that this structural
515 configuration is driven by a recent, large-scale tectonic re-organization of the NE Lau Basin,
516 outlined in **Figure 7**. Prior to ca. 1 Ma, the Tofua Arc formed a relatively continuous chain of
517 volcanoes, oriented $\sim 18\text{--}23^\circ$. The hinge point for large-scale fore-arc rotation was near the
518 Louisville seamount collision at $\sim 175^\circ\text{W}$ and $\sim 24^\circ\text{S}$ (Wallace et al., 2005). Back-arc extension
519 associated with hinge rollback formed the NELSC and MTJ-N parallel to the arc (**Fig. 7a**).
520 While several authors suggest that the FRSC is the most recently formed spreading center in the
521 Lau Basin (e.g., Zellmer & Taylor, 2001), the fact that some of the FRSC segments are NNE-
522 trending (FRSC 4 and 5 in Sleeper et al., 2016) indicates that the proto-FRSC may have started
523 to develop during this time. Wrench tectonics in the northern part of the Lau Basin was driven by
524 transform motion along the STEP boundary that resulted in abundant strike-slip faulting, which
525 was dominated by NNE-trending R' -shears oriented along the extensional fabric of the basin
526 (**Fig. 6a**).

527 Subsequently, the Capricorn Seamount(s) collided with the Tonga trench (**Fig. 7b**). This
528 induced slip in the upper plate at the Fonualei Discontinuity (FD), which segmented the rotating
529 fore-arc block. As the northern block became bound by strike-slip faults, eastward slip along



530
 531 **Figure 7.** Model of the recent tectonic evolution of the NE Lau Basin: (a) prior to collision with the
 532 Capricorn Seamount(s), the trench-arc system was trending NNE, associated with the development of the
 533 NELSC and MTJ-N. Wrench tectonics in the north are driven by transform motion along the STEP and
 534 asymmetric slab rollback (i.e., Model 1 in **Fig. 6**); and (b) collision with the Capricorn Seamount(s) induced
 535 slipping along the Fonualei Discontinuity (FD) adjacent to the collision zone, and caused the northern block
 536 to become bound by strike-slip faults. Eastward movement along the southern FD boundary combined with
 537 westward movement caused by friction along the northern boundary produced an 8–12° counter-clockwise
 538 rotation of stress field. This caused segments of the arc volcanoes to re-orient to a more northerly direction,
 539 and modified the angle of retreat, triggering the propagation of new spreading centers (FRSC, MTJ-S)
 540 as well as smaller propagating faults/rifts in the northern basin. The modified stress field triggered new Riedel
 541 shear mechanisms in the area closest to the arc (i.e., Model 2 in **Fig. 6**) associated with non-rigid plate
 542 kinematics. The new wrench zone boundaries align with the trend of the FD and pre-existing R-shears
 543 produced during earlier Riedel shearing in the wrench zone. Further west of the arc, the original wrench
 544 structures (Model 1) remain seismically active, with a gradual transition to the modified wrench
 545 configuration. Note that the pre-collision size of the Capricorn Seamount(s) is unknown, and the absolute
 546 timing of collision and rift development is poorly constrained. Present day GPS plate vectors from Phillips
 547 (2003).

548 the southern FD boundary may have been accompanied by westward-directed stress along the
549 northern boundary caused by friction. These combined effects promoted a counter-clockwise
550 rotation of the stress field of the northern block by 8–12°. This re-oriented some of the Tofua Arc
551 segments to a more northerly direction (~5–8°), and the reorientation of the extensional axis
552 caused spreading along the MTJ-S and FRSC (**Fig. 7b**). Additional evidence for the development
553 of the FRSC under a changing tectonic regime is provided by Sleeper and Martinez (2016), who
554 link the dynamic history of rotation and opening of the northern Lau Basin with complex
555 asymmetrical structural and volcanic features on the flanks of FRSC. Within the wrench zone,
556 internal plate deformation triggered the formation of Model 2 Riedel shear geometries under this
557 new stress field, primarily affecting the area closest to the arc. In this scenario, the re-activation
558 of faults was favored over the formation of new faults. This work supports the idea that non-rigid
559 plate kinematics are important in the development of the northern Lau Basin, as described by
560 Sleeper and Martinez (2016).

561 A remaining question is whether the collision of an apparently small topographic feature
562 like the Capricorn Seamount(s) can induce such dramatic changes in the stress of the overriding
563 plate. The size of the already-subducted portion of this seamount is unknown, but remaining
564 portion of the seamount rises to ~3200 m from the surrounding seafloor, and the apparent length
565 of the affected trench (indicated by topographic irregularities) is ~60 km (**Fig. 2**, inset). This is
566 comparable to the seamounts that comprise the LSC in the south, which rise to ~3500 m from the
567 surrounding seafloor with trench-parallel widths of ~40–70 km (Ruellan et al., 2003). It is also
568 similar to the size of the d'Entrecasteaux Ridge (DER) that is colliding with the central Vanuatu
569 Arc, which is comprised of two parallel ridges that rise 2–3 km above the surrounding seafloor,
570 with widths of 30–40 km, affecting a total length along the trench of ~115 km (e.g., Collot et al.,

571 1992; Baillard et al., 2018). The effects of the LSC and DER collisions are well-documented,
572 including the effects of plate coupling, locking and unlocking of subduction, arc segmentation,
573 crustal thickening and shortening in the segments adjacent to the collision, reduced back-arc
574 extension, and far-field stresses and associated development of structures (e.g., Charvis &
575 Pelletier, 1989; Meffre & Crawford, 2001; Ruellan et al., 2003; Anderson et al., 2016). In these
576 cases, collision is associated with a strong indentation of the trench and induces rotation of
577 tectonic blocks to the north and/or south of the collision zone (e.g., Wallace et al., 2005; 2009).
578 In contrast, indentation of the trench at the Capricorn collision zone is less pronounced; rather,
579 the predominance of surficial fracturing may result from the ultra-fast subduction rates and/or the
580 size or buoyancy of the subducting seamount(s). This work highlights the importance of terrane
581 collisions in the evolution of subduction zones, which can exert a first-order control on upper
582 plate stresses and associated structures in the back-arc over large areas, providing conduits for
583 magmas to reach the seafloor.

584 6.2. Structural controls on magmatic-hydrothermal activity

585 One of the most striking features of the NE Lau Basin is the decentralized nature of volcanism
586 on the seafloor, manifest by large off-axis volcanic ridges, hydrothermally-active rear-arc
587 volcanoes, and widespread lava flows (**Fig. 3**). Previous authors propose that the Mata rear-arc
588 volcanoes are controlled by small crustal tears linked to strike-slip faulting along the STEP
589 boundary (Govers & Wortel, 2005; Embley et al., 2009), but these authors do not provide an
590 explanation for the variable orientations of the Mata volcanoes, along with other enigmatic
591 features such as the siting of the Niuatahi volcano. The structural framework outlined here
592 provides insight into the occurrence of many of these seafloor features. Notably, large volcanic
593 ridges reflect areas of enhanced magmatism in the map area, and are aligned along several

594 orientations: (1) NNE-trending ridges, including southern Mata volcanoes and the large volcanic
595 ridges at the southern end of the NELSC; (2) E-trending ridges forming the western Mata
596 volcanoes; (3) N-trending ridges, including the large ridge to the north of the FRSC and the
597 subtle ridge extending northward from Niuatahi. In this configuration, NNE- and E-trending
598 features formed early associated with σ_3 extensional structures in the Model 1 configuration (**Fig.**
599 **6a**). These structures were then reactivated as R-shears (Model 2 configuration), along with the
600 formation of the N-trending features during back-arc extension and subsequent re-activation as
601 R'-shears during strike-slip faulting (**Fig. 6b**). In the most recent configuration, extension also
602 occurs along NE-trending structures associated with the new σ_3 orientation. This promotes
603 enhanced magmatism along the southern NELSC and the MTJ-N, as well as rifting along the W
604 Rift zone. We also note that the large Niuatahi rear-arc volcano occurs at the intersection of N-
605 trending and NNE-trending structures. These structures, which have not been previously
606 described, but are underlain by linear magnetic anomalies (Austin, 2012), indicating that magma
607 is exploiting these structural pathways. Dacitic sheet flows at surface extend ~60 km northward
608 from Niuatahi, apparently following a N-trending fissure rather than erupting from the volcano
609 itself (Embley & Rubin, 2018). Within the Niuatahi caldera, hydrothermal vents are also aligned
610 along this N-trending regional structure (**Fig. 3**; Haase et al., 2018). Across the map area,
611 hydrothermal vents are closely associated with these regions of enhanced magmatism. Continual
612 re-activation of faults may ensure that these pathways remain permeable despite precipitation of
613 secondary hydrothermal minerals. This complex structural configuration, combined with
614 unusually high upper mantle temperatures and ultrafast subduction rates (e.g., Regelous, 2008),
615 provides the basis for diverse lithologies and eruption styles in the basin, along with a range of

616 style and composition of hydrothermal venting (e.g., Embley & Rubin, 2018; Chadwick et al.,
617 2019).

618 6.2. Links to microplate emergence

619 Much of our understanding of the emergence of microplates comes from studies in mid-
620 ocean ridge (MOR) settings where plate reorganizations are linked to the propagation of new
621 rifts, forming the boundaries of new microplates (e.g., Wiedicke & Habler, 1993). In contrast,
622 few studies have investigated how these processes operate in back-arc settings where rift
623 propagation is due to subduction-related processes, and the thermal structure of the crust is
624 affected by arc magmatism. Processes such as asymmetric spreading, arc-ward ridge migration,
625 basin-ward arc migration, and the general short-lived nature of spreading centers are common in
626 back-arc basins and less common in MOR settings (e.g., Parson et al., 1990; Martinez and
627 Taylor, 2003). In the NE Lau Basin, we demonstrate the structural effects of a plate
628 reconfiguration associated with the collision of the Capricorn Seamount(s), which has changed
629 the orientation of the extensional axis along a new northward trend. As the extensional axis
630 changes, there is a tendency for rifts to propagate outwards from the tips along the new
631 extensional axis (e.g., CLSC: Parson et al., 1990). This process may be quicker when
632 propagation occurs in thinner crust and where back-arc retreat is the greatest (Parson et al.,
633 1990). The plate reconfiguration associated with the Capricorn Seamount(s) collision may have
634 induced the propagation of new rifts, such as FRSC segments. Simultaneous northward
635 propagation of the FRSC and southward propagation of the MTJ-S produce a zone where the
636 spreading centers overlap, and we observe oblique and curved structural patterns that are
637 characteristic of overlapping spreading centers (North Fiji Basin: Ruellan et al., 1993). Within
638 the map area, major N-trending structures also appear to be extending northward and southward

639 from both tips of the NELSC, and N-trending rifting is occurring along the paleo-arc crust in the
640 northern part of the map area (**Fig. 7b**). These structures may reflect the early stages of rift
641 propagation, but higher-resolution magnetic data is needed to investigate the nature of these
642 features.

643 The re-orientation of the stress field has mainly affected the area closest to the arc,
644 preserving the original wrench zone configuration in the west where it remains seismically active
645 (**Fig. 6**). This suggests that the eastern portion of the NE Lau Basin may be in the nascent stages
646 of nanoplate emergence, proposed by Conder and Wiens (2011) as the separate “Niuatoputapu”
647 plate. This is supported by a drastic change in the structural fabric of the basin from west to east
648 across Escarpment C (**Figs. 3–5**). The fabric to the west of this escarpment is dominated by zig-
649 zagging normal-faulted terrane of the West Rift assemblage, and to the east of this escarpment
650 are the N- and NNE-trending volcanic ridges of the NW Ridge and NELSC assemblages. Like
651 other back-arc micro- and nanoplates, the precise boundaries of Niuatoputapu are difficult to
652 define, and may remain only partially separated, as is the case in the southern diffuse boundary
653 of the Niufo’ou microplate (**Fig. 2**; Sleeper & Martinez, 2016). In back-arc basins, we expect
654 frequent plate reconfigurations associated with seamount collisions. Depending on the stress
655 response in the upper plate, this may provide a mechanism for the generation of mosaics of
656 microplates in back-arc settings (e.g., Mann et al., 1995). However, in the NE Lau Basin this
657 effect may be short-lived and episodic, limited to the duration of the collisional event and
658 associated block movements. It is yet unknown whether a microplate can develop over these
659 short timescales, or if it requires longer-lived processes to fully emerge. Due to the transient
660 nature of this process, it is likely overlooked in the geologic record as kinematic reconstructions
661 are based on magnetic data that may not provide high-enough temporal resolution (e.g., Sleeper

662 & Martinez, 2016). However, this may be an important process in the development of structures
 663 that play a continued role in the magmatic, and hydrothermal evolution of the back-arc.

664 **7. Conclusions**

665 Compared to mid-ocean ridges, back-arc spreading centers are ephemeral features that
 666 evolve dynamically in response to oblique convergence, subduction-zone collisions, and
 667 microplate interactions. The NE Lau Basin is characterized by extreme tectonic complexity,
 668 associated with fast convergence rates, high upper mantle temperatures, and thin oceanic crust
 669 (Bevis, et al., 1995; Conder & Wiens, 2006, Embley, 2018), producing diverse lithologies and
 670 eruption styles in the rear-arc and back-arc regions (e.g., Embley & Rubin, 2018). This
 671 complexity is manifest as seafloor fabrics with variably-oriented structures. The observed
 672 structural patterns reflect the interplay between extension associated with slab-rollback and
 673 strike-slip faulting associated with wrench tectonics along the northern STEP boundary. Two
 674 distinct sets of structures associated with Riedel shear mechanisms are described for the first
 675 time, indicating a recent counter-clockwise rotation of the stress field that primarily affects the
 676 region closest to the arc. The structural configurations highlight the importance of re-activation
 677 of earlier-formed structures during rotation of the stress-field. The structures that formed and
 678 were re-activated in this wrench zone account for the orientations of many of the seafloor
 679 features observed, such as the Mata volcanoes and large off-axis volcanic ridges, providing
 680 additional insight into the tectonic controls on enhanced magmatism along the southern NELSC
 681 and the Niuatahi volcano, as well as the distribution of hydrothermal vent sites in the region. The
 682 rotation of the stress field provides evidence for a large-scale tectonic re-organization of the NE
 683 Lau Basin, which we interpret to be caused by slipping along the Fonualei Discontinuity induced
 684 by the collision of the Capricorn Seamount(s), coupled with westward transform motion along

685 the northern STEP boundary. This plate reconfiguration likely triggered the propagation of
686 FRSC segments, and minor propagation of N-trending faults and rifts in the northernmost back-
687 arc. As seamount collisions are common features of subduction zones, this mechanism for
688 inducing propagating rifts may be important in the formation of new microplates in back-arc
689 settings.

690 **Acknowledgments**

691 Cruise data related to this manuscript is available online: TN234 from Resing et al. (2009);
692 KM1024 from Rubin et al. (2010); KM1129 from Martinez et al. (2013); FK171110 from Rubin
693 et al. (2018); and SO263 from Haase et al. (2018). Supporting information is provided in the
694 electronic appendix associated with this publication. We appreciate the efforts of the SO-263
695 Shipboard Scientific Party, ROV QUEST team, and Captain O. Meyer and his crew on R/V
696 Sonne for their contributions and support. We also thank the FK171110 Shipboard Scientific
697 Party and crew of the R/V Falkor, and the support of the Schmidt Ocean Institute. We gratefully
698 acknowledge S. Panasiuk for her assistance with bathymetric post-processing using the TTS-
699 shader, and L. Calhoun for valuable feedback on the structural interpretations. The funding for
700 the project 03G0263 by the German Bundesministerium für Bildung und Forschung is gratefully
701 acknowledged. MOA acknowledges funding from NSERC-DG and the Connaught New
702 Researcher program (UofT). This is contribution MERC-ME-2020-003 to the modern-ancient
703 crust project of the Canadian Metal Earth program.

704 **References**

- 705 Anderson, M. O., Hannington, M. D., Haase, K., Schwarz-Schampera, U., Augustin, N.,
706 McConachy, T. F., & Allen, K. (2016). Tectonic focusing of voluminous basaltic eruptions in
707 magma-deficient backarc rifts. *Earth and Planetary Science Letters*, *440*, 43–55.
708 <https://doi.org/10.1016/j.epsl.2016.02.002>
- 709 Anderson, M. O., Chadwick, W. W. Jr., Hannington, M. D., Merle, S. G., Resing, J. A., Baker,
710 E. T., Butterfield, D. A., Walker, S. L., & Augustin, N. (2017). Geological interpretation of
711 volcanism and segmentation of the Mariana back-arc spreading center between 12.7°N and
712 18.3°N. *Geochemistry, Geophysics, Geosystems*, *18*, 2240–2274.
713 <https://doi.org/10.1002/2017GC006813>

- 714 Aruculus, R., & Shipboard Scientific Party (2004). Voyage Summary SS06/2004: Submarine
 715 volcanic and hydrothermal activity in the New Hebrides arc-backarc system. *CSIRO Marine*
 716 *Research*. Hobart, Australia: CSIRO. Retrieved from
 717 [http://www.cmar.csiro.au/datacentre/process/data_files/cruise_docs/ss2004_v06_summary.p](http://www.cmar.csiro.au/datacentre/process/data_files/cruise_docs/ss2004_v06_summary.pdf)
 718 [df](http://www.cmar.csiro.au/datacentre/process/data_files/cruise_docs/ss2004_v06_summary.pdf)
- 719 Atmaoui, N., Kukowski, N., Stöckhert, B., & König, D. (2006). Initiation and development of
 720 pull-apart basins with Riedel shear mechanism: insights from scaled clay experiments.
 721 *International Journal of Earth Sciences*, *95*, 225–238. [https://doi.org/10.1007/s00531-005-](https://doi.org/10.1007/s00531-005-0030-1)
 722 [0030-1](https://doi.org/10.1007/s00531-005-0030-1)
- 723 Augustin, N., van der Zwan, F. M., Devey, C. W., Ligi, M., Kwasnitschka, T., Feldens, P.,
 724 Bantan, R. A., & Basaham, A. S. (2016). Geomorphology of the central Red Sea rift:
 725 Determining spreading processes. *Geomorphology*, *274*, 162–179.
 726 <https://doi.org/10.1016/j.geomorph.2016.08.028>
- 727 Austin, R. A. (2012). Early seafloor spreading and variations in crustal accretion in the Lau basin
 728 (Doctoral dissertation). Retrieved from ScholarSpace.
 729 (<https://scholarspace.manoa.hawaii.edu/handle/10125/100916>). Honolulu, HI: University of
 730 Hawai'i at Manoa.
- 731 Baillard, C., Crawford, W. C., Ballu, V., Pelletier, B., Garaebiti, E. (2018). Tracking subducted
 732 ridges through intermediate-depth seismicity in the Vanuatu subduction zone. *Geology*, *46*,
 733 *767–770*. <https://doi.org/10.1130/G45010.1>
- 734 Baker, E. T., Walker, S. L., Massoth, G. J., & Resing, J. A. (2019). The NE Lau Basin:
 735 Widespread and abundant hydrothermal venting in the back-arc region behind a superfast

- 736 subduction zone. *Frontiers in Marine Science*, *6*, 382.
 737 <https://doi.org/10.3389/fmars.2019.00382>
- 738 Baxter, A. T., Hannington, M. D., Stewart, M. S., Emberley, J. M., Breker, K., Krätschell, A.,
 739 Petersen, S., Brandl, P. A., Klischies, M., Mensing, R., & Anderson, M. O. (2020). Shallow
 740 seismicity and the classification of structures in the Lau back-arc basin. Manuscript
 741 submitted for publication.
- 742 Beaulieu, S. E., & Szafranski, K. (2019). InterRidge Global Database of Active Submarine
 743 Hydrothermal Vent Fields, Version 3.4. Retrieved from <http://vents-data.interridge.org>.
- 744 Bevis, M., Taylor, F. W., Schutz, B. E., Recy, J., Isacks, B. L., Helu, S., Singh, R., Kendrick, E.,
 745 Stowell, J., Taylor, B., & Calmantli, S. (1995). Geodetic observations of very rapid
 746 convergence and back-arc extension at the Tonga arc. *Nature*, *374*, 249–251.
 747 <https://doi.org/10.1038/374249a0>
- 748 Bird, P. (2003). An updated digital model of plate boundaries. *Geochemistry, Geophysics,*
 749 *Geosystems*, *4*, 1027. <https://doi.org/10.1029/2001GC000252>
- 750 Bonnardot, M. -A., Régnier, M., Ruellan, E., Christova, C., & Tric, E. (2007). Seismicity and
 751 state of stress within the overriding plate of the Tonga-Kermadec subduction zone. *Tectonics*,
 752 *26*, TC5017. <https://doi.org/10.1029/2006TC002044>
- 753 Brown, L. (2014, April 25). *Texture Shading: A new technique for depicting terrain relief*. Paper
 754 presented at the 15^h ICA Mountain Cartography Workshop, Banff, Canada. Presentation
 755 retrieved from <https://app.box.com/v/textureshading>
- 756 Buck, W. R., Lavier, L. L., & Poliakov, A. N. B. (2005). Modes of faulting at mid-ocean ridges.
 757 *Nature*, *434*, 719–723. <https://doi.org/10.1038/nature03358>

- 758 Byerlee, J. D. (1978). Friction of rocks. *Pure and Applied Geophysics*, *116*, 615–626.
 759 <https://doi.org/10.1007/BF00876528>
- 760 Tontini, F. C., Bassett, D., de Ronde, C. E. J., Timm, C., & Wysoczanski, R. (2019). Early
 761 evolution of a young back-arc basin in the Havre Trough. *Nature Geoscience*, *12*, 856–862.
 762 <https://doi.org/10.1038/s41561-019-0439-y>
- 763 Chadwick, W. W. Jr., Rubin, K. H., Merle, S. G., Bobbitt, A. M., Kwasnitschka, T., & Embley,
 764 R. W. (2019). Recent eruptions between 2012–2018 discovered at West Mata submarine
 765 volcano (NE Lau Basin, SW Pacific) and characterized by new ship, AUV, and ROV data.
 766 *Frontiers in Marine Science*, *6*, 495. <https://doi.org/10.3389/fmars.2019.00495>
- 767 Charvis, P., & Pelletier, B. (1989). The northern New Hebrides back-arc troughs: history and
 768 relation with the North Fiji Basin. *Tectonophysics*, *170*, 259–277.
 769 [https://doi.org/10.1016/0040-1951\(89\)90275-8](https://doi.org/10.1016/0040-1951(89)90275-8)
- 770 Chase, C. G. (1978). Extension behind island arcs and motions relative to hot spots. *Journal of*
 771 *Geophysical Research: Solid Earth*, *83*(B11), 5385–5387.
 772 <https://doi.org/10.1029/JB083iB11p05385>
- 773 Conder, J. A., & Wiens, D. A. (2011). Shallow seismicity and tectonics of the central and
 774 northern Lau Basin. *Earth and Planetary Science Letters*, *304*, 538–546.
 775 <https://doi.org/10.1016/j.epsl.2011.02.032>
- 776 Collot, J. Y., Lallemand, S., Pelletier, B., Eissen, J. -P., Glaçon, G., Fisher, M. A., Greene, H. G.,
 777 Boulin, J., Daniel, J., & Monzier, M. (1992). Geology of the d'Entrecasteaux-New Hebrides
 778 Arc collision zone: results from a deep submersible survey. *Tectonophysics*, *212*, 213–241.
 779 [https://doi.org/10.1016/0040-1951\(92\)90292-E](https://doi.org/10.1016/0040-1951(92)90292-E)

- 780 Dziewonski, A. M., Chou, T. -A., & Woodhouse, J. H. (1981). Determination of earthquake
 781 source parameters from waveform data for studies of global and regional seismicity. *Journal*
 782 *of Geophysical Research: Solid Earth*, 86(B4), 2825–2852.
 783 <https://doi.org/10.1029/JB086iB04p02825>
- 784 Ekström, G., Nettles, M., & Dziewoński, A. M. (2012). The global CMT project 2004–2010:
 785 Centroid-moment tensors for 13,017 earthquakes. *Physics of the Earth and Planetary*
 786 *Interiors*, 200–201, 1–9. <https://doi.org/10.1016/j.pepi.2012.04.002>
- 787 Embley, R. W., Merle, S. G., Lupton, J. E., Resing, J., Baker, E. T., Lilley, M. D., Arculus, R. J.,
 788 & Crowhurst, P. V. (2009). *Extensive and Diverse Submarine Volcanism and Hydrothermal*
 789 *Activity in the NE Lau Basin*. Paper presented at the American Geophysical Union Fall
 790 Meeting 2009, San Francisco, CA. Abstract retrieved from
 791 <https://ui.adsabs.harvard.edu/abs/2009AGUFM.V51D1719E/abstract>
- 792 Embley, R. W., & Rubin, K. H. (2018). Extensive young silicic volcanism produces large deep
 793 submarine lava flows in the NE Lau Basin. *Bulletin of Volcanology*, 80, 36.
 794 <https://doi.org/10.1007/s00445-018-1211-7>
- 795 Escrig, S., Bézoz, A., Langmuir, C. H., Michael, P. J., & Arculus, R. (2012). Characterizing the
 796 effect of mantle source, subduction input and melting in the Fonualei Spreading Center, Lau
 797 Basin: Constraints on the origin of the boninitic signature of the back-arc lavas.
 798 *Geochemistry, Geophysics, Geosystems*, 13, Q10008.
 799 <https://doi.org/10.1029/2012GC004130>.

- 800 Falloon, T. J., Malahoff, A., Zonenshaina, L. P., & Bogdanova, Y. (1992). Petrology and
 801 geochemistry of back-arc basin basalts from Lau Basin spreading ridges at 15°, 18° and
 802 19°S. *Mineralogy and Petrology*, *47*, 1–35. <https://doi.org/10.1007/BF01165295>
- 803 Falloon, T. J., Danyushevsky, L. V., Crawford, T. J., Maas, R., Woodhead, J. D., Eggins, S. M.,
 804 Bloomer, S. H., Wright, D. J., Zlobin, S. K., & Stacey, A. R. (2007). Multiple mantle plume
 805 components involved in the petrogenesis of subduction-related lavas from the northern
 806 termination of the Tonga arc and northern Lau Basin: Evidence from the geochemistry of arc
 807 and backarc submarine volcanics. *Geochemistry, Geophysics, Geosystems*, *8*, Q09003.
 808 <https://doi.org/10.1029/2007GC001619>
- 809 GEBCO Compilation Group (2019). GEBCO 2019 Grid [dataset]. doi:10.5285/836f016a-33be-
 810 6ddc-e053-6c86abc0788e
- 811 Global Volcanism Program (2013). *Volcanoes of the World*, v. 4.8.6. Venzke, E (ed.).
 812 Smithsonian Institution. Retrieved from <https://doi.org/10.5479/si.GVP.VOTW4-2013>
- 813 Govers, R., & Wortel, M. (2005). Lithosphere tearing at step faults: Response to edges of
 814 subduction zones. *Earth and Planetary Science Letters*, *236*, 505–523.
 815 <https://doi.org/10.1016/j.epsl.2005.03.022>
- 816 Haase, K., & Shipboard Scientific Party (2018). SO-263 cruise report Tonga Rift.
 817 *Wochenberichte und short cruise reports*. Hamburg, Germany: Universität Hamburg.
 818 Retrieved from [https://www.ldf.uni-hamburg.de/sonne/wochenberichte/wochenberichte-
 819 sonne/so263-265/so263-scr.pdf](https://www.ldf.uni-hamburg.de/sonne/wochenberichte/wochenberichte-sonne/so263-265/so263-scr.pdf)

- 820 Hall, R. (2002). Cenozoic geological and plate tectonic evolution of SE Asia and the SE Pacific:
 821 computer-based reconstructions, model and animations. *Journal of Asian Earth Science*, 20,
 822 353–431. [https://doi.org/10.1016/S1367-9120\(01\)00069-4](https://doi.org/10.1016/S1367-9120(01)00069-4)
- 823 Hall, R., & Spakman, W. (2002). Subducted slabs beneath the eastern Indonesia-Tonga region:
 824 Insights from tomography. *Earth and Planetary Science Letters*, 201, 321–336.
 825 [https://doi.org/10.1016/S0012-821X\(02\)00705-7](https://doi.org/10.1016/S0012-821X(02)00705-7)
- 826 Hawkins, J. W. (1995). The geology of the Lau Basin. In B. Taylor (Ed.), *Backarc Basins:
 827 Tectonics and Magmatism* (pp. 63–138). New York, NY: Plenum Press.
- 828 Heuret, A., & Lallemand, S. (2005). Plate motions, slab dynamics and back-arc deformation.
 829 *Physics of the Earth and Planetary Interiors*, 149, 31–51.
 830 <https://doi.org/10.1016/j.pepi.2004.08.022>
- 831 Hey, R. N., Johnson, P., Martinez, F., Korenaga, J., Somers, M., Hugget, Q., LeBas, T., Rusby,
 832 R., & Naar, D. (1995). Plate boundary reorganization at a large-offset, rapidly propagating
 833 rift. *Nature*, 378, 167–170. <https://doi.org/10.1038/378167a0>
- 834 Ito, G., & Behn, M. D. (2008). Magmatic and tectonic extension at mid-ocean ridges: 2. Origin
 835 of axial morphology. *Geochemistry, Geophysics, Geosystems*, 9, Q09O12.
 836 <https://doi.org/10.1029/2008GC001970>
- 837 Karig, D. E. (1970). Ridges and basins of the Tonga-Kermadec island arc system. *Journal of
 838 Geophysical Research*, 75, 239–254. <https://doi.org/10.1029/JB075i002p00239>
- 839 Keller, N. S., Arculus, R. J., Hermann, J., & Richards, S. (2008). Submarine back-arc lava with
 840 arc signature: Fonualei Spreading Center, northeast Lau Basin, Tonga. *Journal of
 841 Geophysical Research: Solid Earth*, 113, B08S07. <https://doi.org/10.1029/2007JB005451>

- 842 Kim, J., Son, J. -W., Kim, K. -H., Shim, W. J., Kim, C. H., Lee, K. -Y. (2009). Venting sites
 843 along the Fonualei and Northeast Lau Spreading Centers and evidence of hydrothermal
 844 activity at an off-axis caldera in the northeastern Lau Basin. *Geochemical Journal*, *43*, 1–13.
 845 <https://doi.org/10.2343/geochemj.0.0164>
- 846 Klischies, M., Petersen, S., & Devey, C. W. (2019). Geological mapping of the Menez Gwen
 847 segment at 37°50'N on the Mid-Atlantic Ridge: Implications for accretion mechanisms and
 848 associated hydrothermal activity at slow-spreading mid ocean ridges. *Marine Geology*, *412*,
 849 107–122. <https://doi.org/10.1016/j.margeo.2019.03.012>
- 850 Langmuir, C. H., Bézos, A., Escrig, S., & Parman, S. W. (2006). Chemical Systematics and
 851 Hydrous Melting of the Mantle in Back-Arc Basins. In D. M. Christie, C. R. Fisher, S. -M.
 852 Lee, & Givens, S. (Eds.). *Back-Arc Spreading Systems: Geological, Biological, Chemical,*
 853 *and Physical Interactions* (Vol. 166, pp. 87–146. Washington, DC:American Geophysical
 854 Union, Geophysical Monograph Series. <https://doi.org/10.1029/166GM07>
- 855 Lupton, J., Rubin, K. H., Arculus, R., Lilley, M., Butterfield, D., Resing, J., et al. (2015). Helium
 856 isotope, He, and Ba-Nb-Ti signatures in the northern Lau Basin: Distinguishing arc, back-arc,
 857 and hotspot affinities: Helium and Carbon in Northern Lau Basin. *Geochemistry, Geophysics,*
 858 *Geosystems*, *16*, 1133–1155. <https://doi.org/10.1002/2014GC005625>
- 859 Maestro-González, A., Bárcenas, P., Vázquez, J. T., & Díaz-del-Río, V. (2008). The role of
 860 basement inheritance faults in the recent fracture system of the inner shelf around Alboran
 861 Island, Western Mediterranean. *Geo-Marine Letters*, *28*, 53–64.
 862 <https://doi.org/10.1007/s00367-007-0089-8>

- 863 Martinez, F., & Taylor, B. (1996). Backarc spreading, rifting, and microplate rotation, between
 864 transform faults in the Manus Basin. *Marine Geophysical Researches*, *18*, 203–224.
 865 <https://doi.org/10.1007/BF00286078>
- 866 Martinez, F., & Taylor, B. (2003). Controls on back-arc crustal accretion: Insights from the Lau,
 867 Manus and Mariana basins. In R. D. Larter & P. T. Leat (Eds.). *Intra-Oceanic Subduction*
 868 *Systems: Tectonic and Magmatic Processes* (Vol. 219, pp. 19–54). London, UK: The
 869 Geological Society of London, Special Publications.
 870 <https://doi.org/10.1144/GSL.SP.2003.219.01.02>
- 871 Martinez, F., & Shipboard Scientific Party (2013). R/V Kilo Moana KM1129 [cruise data].
 872 Available from *Rolling Deck to Repository (R2R)*: <https://doi.org/10.7284/903698>
- 873 Mallard, C., Coltice, N., Seton, M., Müller, R. D., & Tackley, P.J. (2016). Subduction controls
 874 the distribution and fragmentation of Earth’s tectonic plates. *Nature*, *535*, 140–143.
 875 <https://doi.org/10.1038/nature17992>
- 876 Mann, P., Taylor, F. W., Edwards, R. L., Ku, T. -K. (1995). Actively evolving microplate
 877 formation by oblique collision and sideways motion along strike-slip faults: An example
 878 from the northeastern Caribbean plate margin. *Tectonophysics*, *246*, 1–69.
 879 [https://doi.org/10.1016/0040-1951\(94\)00268-E](https://doi.org/10.1016/0040-1951(94)00268-E)
- 880 McKenzie, D. P. (1969). The relation between fault plane solutions for earthquakes and the
 881 directions of the principal stresses. *Bulletin of the Seismological Society of America*, *59*, 591–
 882 601.
- 883 Meffre, S., & Crawford, A. J. (2001). Collision tectonics in the New Hebrides arc (Vanuatu). *The*
 884 *Island Arc*, *10*, 33–50. <https://doi.org/10.1046/j.1440-1738.2001.00292.x>

- 885 Millen, D. W., & Hamburger, M. W. (1998). Seismological evidence for tearing of the Pacific
 886 Plate at the northern termination of the Tonga subduction zone. *Geology*, *26*, 659–662.
 887 [https://doi.org/10.1130/0091-7613\(1998\)026<0659:SEFTOT>2.3.CO;2](https://doi.org/10.1130/0091-7613(1998)026<0659:SEFTOT>2.3.CO;2)
- 888 Morley, C. K., Haranya, C., Phoosongsee, W., Pongwapee, S., Kornsawan, A., & Wongan, N.
 889 (2004). Activation of rift oblique and rift parallel pre-existing fabrics during extension and
 890 their effect on deformation style: examples from the rifts of Thailand. *Journal of Structural*
 891 *Geology*, *26*, 1803–1829. <https://doi.org/10.1016/j.jsg.2004.02.014>
- 892 Neves, M., Searle, R., & Bott, M. (2003). Easter microplate dynamics. *Journal of Geophysical*
 893 *Research: Solid Earth*, *108*, 2213. <https://doi.org/10.1029/2001JB000908>
- 894 Nijholt, N., & Govers, R. (2015). The role of passive margins on the evolution of subduction-
 895 transform edge propagators (STEPs). *Journal of Geophysical Research: Solid Earth*, *120*,
 896 7203–7230. <https://doi.org/10.1002/2015JB012202>
- 897 Nilsson, K., Florendo, F., & Hawkins, J. W. (1989). Petrology of a nascent triple junction,
 898 northeastern Lau Basin. *Eos*, *73*, 1389.
- 899 Park, J. -W., Campbell, I. H., Kim, J., Moon, J. -W. (2015). The role of late sulfide saturation in
 900 the formation of a Cu- and Au-rich magma: Insights from the platinum group element
 901 geochemistry of Niutahi-Motutahi lavas, Tonga rear arc. *Journal of Petrology*, *56*, 59–81.
 902 <https://doi.org/10.1093/petrology/egu071>
- 903 Parson, L., Pearce, J. A., Murton, B., & Hodkinson, R. (1990). Role of ridge jumps and ridge
 904 propagation in the tectonic evolution of the Lau back-arc basin, southwest Pacific. *Geology*,
 905 *18*, 470–473. [https://doi.org/10.1130/0091-7613\(1990\)018<0470:RORJAR>2.3.CO;2](https://doi.org/10.1130/0091-7613(1990)018<0470:RORJAR>2.3.CO;2)

- 906 Pelletier, B., Lagabrielle, Y., Benoit, M., Cabioch, G., Calmant, S., & Garel, E. (2001). Newly
 907 identified segments of the Pacific-Australia plate boundary along the North Fiji transform
 908 zone. *Earth and Planetary Science Letters*, *193*, 347–358. <https://doi.org/10.1016/S0012->
 909 821X(01)00522-2
- 910 Phillips, D. A. (2003). Crustal motion studies in the Southwest Pacific: Geodetic measurements
 911 of plate convergence in Tonga, Vanuatu and the Solomon Islands (Doctoral dissertation).
 912 Retrieved from ProQuest. (<https://search.proquest.com/docview/305327521>). Honolulu, HI:
 913 University of Hawai’i at Manoa.
- 914 Regelous, M., Turner, S., Falloon, T. J., Taylor, P., Gamble, J., & Green, T. (2008). Mantle
 915 dynamics and melting beneath Niufo’ou Island and the northern Lau back-arc basin.
 916 *Contributions to Mineralogy and Petrology*, *156*, 103–118. <https://doi.org/10.1007/s00410->
 917 007-0276-7
- 918 Resing, J., & Shipboard Scientific Party (2009). R/V Thomas G. Thompson TN234 [cruise data].
 919 Available from *Rolling Deck to Repository (R2R)*: <https://doi.org/10.7284/903993>
- 920 Resing, J. A., Baker, E. T., Lupton, J. E., Lilley, M. D., Rubin, K. H., & Buck, N. J. (2011a,
 921 December 5–9). *The Chemistry of Hydrothermal venting at a Volcano “O”, a large*
 922 *Submarine Volcano in the NE Lau Basin*. Paper presented at the American Geophysical
 923 Union Fall Meeting 2011, San Francisco, CA. Abstract retrieved from
 924 <https://ui.adsabs.harvard.edu/abs/2011AGUFM.V53D2652R/abstract>
- 925 Resing, J. A., Rubin, K. H., Embley, R. W., Lupton, J. E., Baker, E. T., Dziak, R. P.,
 926 Baumberger, T., Lilley, M. D., Huber, J. A., Shank, T. M. et al. (2011b). Active submarine

- 927 eruption of boninite in the northeastern Lau Basin. *Nature Geoscience*, 4, 799–806.
- 928 <https://doi.org/10.1038/ngeo1275>
- 929 Rubin, K., & Shipboard Scientific Party (2010). R/V Kilo Moana KM1024 [cruise data].
- 930 Available from *Rolling Deck to Repository (R2R)*: <https://doi.org/10.7284/900840>
- 931 Rubin, K., & Embley, R. (2012). *Identification and implications of a submarine monogenetic*
- 932 *field in the NE Lau Basin*. Paper presented at the American Geophysical Union Fall Meeting
- 933 2012, San Francisco, CA. Abstract retrieved from
- 934 <https://ui.adsabs.harvard.edu/abs/2012AGUFM.V44C..08R/abstract>
- 935 Rubin, K., Embley, R., Arculus, R., & Lupton, J. (2013). *Magmatically greedy rear-arc*
- 936 *volcanoes of the N. Tofua segment of the Tonga arc*. Paper presented at the American
- 937 Geophysical Union Fall Meeting 2013, San Francisco, CA. Abstract retrieved from
- 938 <https://ui.adsabs.harvard.edu/abs/2013AGUFM.V13I..04R/abstract>
- 939 Rubin, K. H., & Embley, R. W. (2016). Tectonic and volcanic interplays in earths largest and
- 940 only known active boninite volcano province. *Geological Society of America Abstracts with*
- 941 *Programs*, 48(7). <https://doi.org/10.1130/abs/2016AM-286764>.
- 942 Rubin, K., & Shipboard Scientific Party (2018). R/V Falkor FK171110 [cruise data]. Available
- 943 from *Rolling Deck to Repository (R2R)*: <https://doi.org/10.7284/907642>
- 944 Ruellan, E., Delteil, J., Wright, I., & Matsumoto, T. (2003). From rifting to active spreading in
- 945 the Lau Basin - Havre trough backarc system (SW Pacific): Locking/unlocking induced by
- 946 seamount chain subduction. *Geochemistry, Geophysics, Geosystems*, 4, 8909.
- 947 <https://doi.org/10.1029/2001GC000261>

- 948 Scholz, C., & Campos, J. (1995). On the mechanism of seismic decoupling and back arc
 949 spreading at subduction zones. *Journal of Geophysical Research: Solid Earth*, *100*, 22103–
 950 22115. <https://doi.org/10.1029/95JB01869>
- 951 Schouten, H., Klitgord, K. D., & Gallo, D. G. (1993). Edge-driven microplate kinematics.
 952 *Journal of Geophysical Research: Solid Earth*, *98*, 6689–6701.
 953 <https://doi.org/10.1029/92JB02749>
- 954 Sdrolias, M., & Muller, R. D. (2006). Controls on back-arc basin formation. *Geochemistry,*
 955 *Geophysics, Geosystems*, *7*, Q04016. <https://doi.org/10.1029/2005GC001090>
- 956 Sleeper, J. D. (2017). Tectonic and Magmatic Controls on Extension and Crustal accretion in
 957 Backarc Basins, Insights from the Lau Basin and Southern Mariana Trough (Doctoral
 958 dissertation). Retrieved from SOEST.
 959 (https://www.soest.hawaii.edu/GG/academics/theses/Sleeper_Dissertation.pdf). Honolulu,
 960 HI: University of Hawai'i at Manoa.
- 961 Sleeper, J. D., & Martinez, F. (2016). Geology and kinematics of the Niufo'ou microplate in the
 962 northern Lau Basin. *Journal of Geophysical Research: Solid Earth*, *121*, 4852–4875.
 963 <https://doi.org/10.1002/2016JB013051>
- 964 Sleeper, J. D., Martinez, F., & Arculus, R. (2016). The Fonualei Rift and Spreading Center:
 965 Effects of ultraslow spreading and arc proximity on back-arc crustal accretion. *Journal of*
 966 *Geophysical Research: Solid Earth*, *121*, 4814–4835. <https://doi.org/10.1002/2016JB013050>
- 967 Stratford, W., Peirce, C., Paulatto, M., Funnell, M., Watts, A. B., Grevemeyer, I., & Bassett, D.
 968 (2015). Seismic velocity structure and deformation due to the collision of the Louisville

- 969 Ridge with the Tonga-Kermadec Trench. *Geophysical Journal International*, *200*, 1503–
 970 1522. <https://doi.org/10.1093/gji/ggu475>
- 971 Tappin, D., Bruns, T., & Geist, E. (1994). Rifting of the Tonga/Lau ridge and formation of the
 972 Lau backarc basin: Evidence from site 840 on the Tonga Ridge. In J. Hawkins, L. Parson, J.
 973 Allan, et al. (Eds.) *Proceedings of the Ocean Drilling Program, Scientific Results* (Vol. 135,
 974 pp. 367–371). College Station, TX: Ocean Drilling Program.
- 975 Taylor, B., Zellmer, K., Martinez, F., & Goodliffe, A. (1996). Sea-floor spreading in the Lau
 976 back-arc basin. *Earth and Planetary Science Letters*, *144*, 35–40.
 977 [https://doi.org/10.1016/0012-821X\(96\)00148-3](https://doi.org/10.1016/0012-821X(96)00148-3)
- 978 Taylor, P.W., & Ewart, A. (1997). The Tofua volcanic arc, Tonga, SW Pacific: Review of
 979 historic volcanic activity. Australian Volcanological Investigations (AVI) Occasional Report
 980 No. 97/01. Pymble, New South Wales: Australian Volcanological Investigations.
- 981 Tian, L., Castillo, P. R., Hilton, D. R., Hawkins, J. W., Hanan, B. B., & Pietruszka, A. J. (2011).
 982 Major and trace element and Sr-Nd isotope signatures of the northern Lau Basin lavas:
 983 Implications for the composition and dynamics of the back-arc basin mantle. *Journal of*
 984 *Geophysical Research: Solid Earth*, *116*, B11201. <https://doi.org/10.1029/2011JB008791>
- 985 Todd, E., Gill, J. B., Wysoczanski, R. J., Handler, M. R., Wright, I. C., & Gamble, J. A. (2010).
 986 Sources of constructional cross-chain volcanism in the southern Havre Trough: New insights
 987 from HFSE and REE concentration and isotope systematics. *Geochemistry, Geophysics,*
 988 *Geosystems*, *11*, Q04009. <https://doi.org/10.1029/2009GC002888>

- 989 van Keken, P. E., Hacker, B. R., Syracuse, E. M., & Abers, G. A. (2011). Subduction factory: 4.
 990 Depth-dependent flux of H₂O from subducting slabs worldwide. *Journal of Geophysical*
 991 *Research: Solid Earth*, 116, B01401. <https://doi.org/10.1029/2010JB007922>.
- 992 Wallace, L. M., Beavan, J., McCaffrey, R., & Darby, D. (2004). Subduction zone coupling and
 993 tectonic block rotations in the North Island, New Zealand. *Journal of Geophysical Research:*
 994 *Solid Earth*, 109, B12406. <https://doi.org/10.1029/2004JB003241>
- 995 Wallace, L. M., McCaffrey, R., Beavan, J., Ellis, S. (2005). Rapid microplate rotations and
 996 backarc rifting at the transition between collision and subduction. *Geology*, 33, 857–860.
 997 <https://doi.org/10.1130/G21834.1>
- 998 Wallace, L. M., Ellis, S., & Mann, P. (2009). Collisional model for rapid fore-arc block rotations,
 999 arc curvature, and episodic back-arc rifting in subduction settings. *Geochemistry,*
 1000 *Geophysics, Geosystems*, 10, Q05001. <https://doi.org/10.1029/2008GC002220>
- 1001 Wiedicke, M., & Collier, J. (1993). Morphology of the Valu Fa spreading ridge in the southern
 1002 Lau basin. *Journal of Geophysical Research: Solid Earth*, 98, 11769–11782.
- 1003 Wiedicke, M., & Habler, W. (1993). Morphotectonic characteristics of a propagating spreading
 1004 system in the northern Lau Basin. *Journal of Geophysical Research: Solid Earth*, 98,
 1005 11,783–11,797. <https://doi.org/10.1029/93JB00707>
- 1006 Wysoczanski, R., Leonard, G., Gill, J., Wright, I., Calvert, A., McIntosh, W., Jicha, B., Gamble,
 1007 J., Timm, C., Handler, M., Drewes-Todd, E., & Zohrab, A. (2019). Ar-Ar age constraints on
 1008 the timing of Havre Trough opening and magmatism. *New Zealand Journal of Geology and*
 1009 *Geophysics*, 62, 371–377. <https://doi.org/10.1080/00288306.2019.1602059>

- 1010 Zellmer, K. E., & Taylor, B. (2001). A three-plate kinematic model for Lau Basin opening.
1011 *Geochemistry, Geophysics, Geosystems*, 2. <https://doi.org/10.1029/2000GC000106>
- 1012 Zhang, H., Yan, Q., Li, C., Zhu, Z., Zhao, R., & Shi, X. (2018). Geochemistry of diverse lava
1013 types from the Lau Basin (SW Pacific): Implications for complex back-arc mantle dynamics.
1014 *Geological Journal*, 54, 3643–3659. <https://doi.org/10.1002/gj.3354>